Master's thesis

Degree Programme in Physical Sciences

Physics

X-ray Microtomography Measurements of Bioactive Glass Scaffolds in Rabbit Femur Samples at Multiple Stages of Bone Regeneration: Reduction of Image Artefacts and a Preliminary Segmentation

Vesa-Matti Leino

November 30, 2020

Supervisors:	PhD Heikki Suhonen
	PhD Nina C. Lindfors
Examiners:	PhD Heikki Suhonen
	PhD Nina C. Lindfors
	PhD Simo Huotari

UNIVERSITY OF HELSINKI
FACULTY OF SCIENCE

Tiivistelmä — Referat — Abstract

A series of x-ray microtomography (μCT) measurements was performed on a set of rabbit femur bone samples containing artificial scaffolds of bioactive glass BAG-S53P4, implanted into an intentionally induced defect, i.e. a gap, in the femur. The scaffolds, some additionally enveloped in PLGA, were supportive structures composed of small granules of bioactive glass, intended to enhance, stimulate and guide the healing and regeneration of bone. The 34 samples were harvested from the rabbits at three different stages of healing and bone regeneration: 2 weeks, 4 weeks and 8 weeks. In addition to 27 samples that contained scaffolds of BAG-S53P4 or BAG-S53P4-PLGA, which had been implanted into the femur of a rabbit, 3 scaffolds of BAG-S53P4(-PLGA) that were not implanted and 7 control samples containing inert PMMA-implants were also included in the measurements for comparison.

During the healing process the bioactive glass granules are gradually dissolved into the surrounding bodily fluids and a thin reaction layer composed of silica gel forms onto the surfaces of the granules. Subsequently an additional surface layer composed of HCA, a material that closely resembles natural hydroxyapatite, is formed onto the granules. As the healing process to regenerate the bone in the gap progresses, a complex three-dimensional network of newly formed trabecular bone grows in between the granules, attaching onto the surface layers and eventually enveloping the gradually dissolving granules entirely. Ultimately, the scaffold is intended to degrade completely, and a structure of regenerated, remodeled cortical bone is expected to be formed into the volume of the initial defect.

As the thicknesses of both the surface layers of the granules and the individual trabeculae of the newly formed bone are in the micrometre range, x-ray microtomography was employed to evaluate and assess the complex three-dimensional structure, consisting of trabecular bone intertwined with granules at varying stages of dissolution. By evaluating the rate of formation of these structures at three different stages, i.e. time points, of regeneration, valuable information on the effectiveness of the bioactive glass BAG-S53P4(-PLGA) for the regeneration of defected bone can be obtained.

The measurements were performed at University of Helsinki's Laboratory of Microtomography using its Nanotom-apparatus with 80kV voltage, 150μA current and a voxel size of 15μm^3. 1000 projection images per sample were used in 37 reconstructions utilizing the FBP-algorithm. Subsequent image processing to analyze and compare the samples was conducted using ImageJ. A procedure to reduce image artefacts – due to metal parts in the samples – was developed, utilizing Gaussian filtering, as well as a preliminary image segmentation scheme, utilizing Morphological filtering, to automatically separate the bone from the granules and their surface layers.

List of Figures

List of Tables

Contents

Part I

Introduction

1. Introduction

This Master's Thesis in Physics has its origin in a wider Medical research project that investigates a relatively novel biologically compatible material, a *bioactive glass* of type S53P4, intended to enhance the healing process and promote the *regeneration* of injured bone. The Thesis includes a description of a series of measurements performed on a *set* of bone samples containing the material, conducted to determine the internal structure of the samples in detail. The scanned internal structures of the samples will then be illustrated in multiple images that are created on the basis of the measurements, and finally a preliminary analysis of the results, obtained by processing the images further, is presented. In addition, a thorough description of the theoretical background of both the measurements and the samples, and also of the image processing methods, is given.

The series of measurements was conducted using *x-ray microtomography*, a technique which is conventionally employed in the field of *materials science* [1][2]. The set of samples, however, consisted of *biological* and biologically compatible materials, i.e. bone and granules of bioactive glass embedded amid each other, designed to eventually fuse and merge together to form a thoroughly regenerated biological structure [3]. The samples were originally harvested at different stages of biological development, and due to disparities in the rates of the regenerative process, the exact *chemical* composition of their constituent materials varied amongst the samples [4]. Furthermore, the ultimate objective of the series of measurements was to aid in the assessment of the potential *medical* benefits that presumably would result from the utilization of the biologically compatible (*biocompatible*) material, the bioactive glass of type and composition S53P4 (containing, as a percentage by weight, 53% silicon SiO_2 and 4% phosphorus P_2O_5) [5].

This type of multi- or interdisciplinary approach to the subject of research, the bioactive glass, combines the contributions from multiple fields of research, i.e. physical, chemical, biological and medical research, to achieve results that would otherwise be unattainable [3]. Principally the research on this particular type of bioactive glass, S53P4, is conducted by medical research teams [5], but as a part of a larger project, involving the measurement and *imaging* of samples from rabbit femurs, the techniques and methods of materials science were estimated to be well suited for the task. The method of choice was x-ray microtomography, as it has a potential resolution several

orders of magnitude higher than standard medical equipment, for example that of a standard medical CT-scan (i.e. *conventional* x-ray computed tomography) [3]. Similar to a standard medical CT-scan, x-ray microtomography has the intrinsic benefit that the sample does not need to be dissected, stained or otherwise impaired prior to the measurements [6]. The fundamental *difference* between conventional x-ray computed tomography and x-ray (computed) *micro*tomography is the minute sample *size* of the latter, enabling a magnification (in effect a resolution) orders of magnitude greater [1].

X-ray microtomography is a well-established and extensively utilized method of materials science for scanning the internal structure of materials at a length scale of *micro*metres ($\mu m = 1 \cdot 10^{-6} m$), a unit of length that is defined as one millionth of a metre in magnitude [1]. The method – often also referred to as x-ray micro-computed tomography (μCT) [7] – combines the intrinsic accuracy, precision and penetrative power of x-ray radiation with the refined algorithms of computed tomography [8][9], resulting in the formation of an essentially three-dimensional image – a *model* – of the entire scanned object [10][11]. The three-dimensional (3D) image may be viewed from any direction necessary [6] and in addition be sectioned or segmented as needed [6], enabling any cross-sectional area of the sample to be revealed. As the resolution of the 3D-image is in the micrometre length scale, many of the most elaborate structural features of the material's interior can then – in principle – be evaluated in a relatively straightforward manner [12].

At the length scale of micrometres, materials often form complex structures that are *fundamentally three-dimensional* in character, for example *porous* formations that resemble solid foam [13], or intricate *networks* consisting of thin strands of matter [14]. Alongside the various materials that spontaneously adopt a complex three-dimensional configuration at the *micrometre range* of approximately $0.1 \ldots 100 \mu m$ ($10^{-7} \ldots 10^{-4} m$), a particularly relevant class of materials comprises those that are created by biological processes inside living organisms, i.e. *biological materials* [13]. Among the plethora of biological materials that have a tendency to form complex three-dimensional structures at the micrometre length scale, one of the most important materials to consider is *bone*, either human bone or analogous bone of some other species, for example rabbit [3].

1.1   The Healing Process of Bone

Bone generally has *two* distinct forms, or three-dimensional structures, to which it grows into: *cortical* bone and *trabecular* bone [15]. Of these, cortical bone is the type of hard and compact bone that is familiar from the long bones of human anatomy [15], for example the exterior side of a human femur is mainly composed of cortical bone [15]. This form – or *growth pattern* – of bone is uniformly dense within the entire volume it

grows into [15], apart from the canals, vessels and certain other minuscule anatomical features that the bone naturally contains [16]. Of the two types of growth patterns, cortical bone is far more common, and constitutes the main supporting framework for the rest of the body [15].

The second, yet equally important type of bone is the trabecular, or *cancellous*, bone, which adopts a fundamentally different growth pattern as compared to cortical bone [7]. In a marked contrast to the uniform and consistently dense structure of cortical bone, trabecular bone forms instead an intricate three-dimensional *network* of interconnected segments of bone, with relatively large *cavities* between them [7]. The length scale to which these individual segments of bone, the *trabeculae*, grow into is in the micrometre range, varying from approximately $30 \ldots 300$µm ($3 \cdot 10^{-5} \ldots 3 \cdot 10^{-4}$m), above which the structure can in turn be regarded as cortical bone, since both types of structures are composed of essentially the same material, their difference lying in the three-dimensional growth pattern – the *morphology* [17] – that the bone has adopted.

Bone is a biological material – a living tissue to be exact – composed primarily of mineralized substances embedded in a *matrix* of organic, mainly collagen, fibrils [16]. As a living tissue [15], bone also contains an abundance of living cells, a complicated architecture of blood vessels and a multitude of other types of anatomical features [16], in addition to the actual *bone mineral* and the surrounding matrix [15]. Both cortical and trabecular bone are mainly composed of this same biological material, which has the physical properties of being hard and relatively resilient to fracture [16]. Despite the inherent thinness of the individual trabeculae, the three-dimensional overall structure of trabecular bone enables it to be simultaneously lightweight and relatively strong, yet at the same time reasonably flexible [17]. A feature that is equally important in terms of the *chemical* and biological properties of trabecular bone is the added *surface area* of the structure, which enables considerably more biological interaction with blood and other bodily fluids to take place [17].

Trabecular bone can ordinarily be found – predominantly – on the *interior* of the long bones and the spinal *vertebrae*, often adjacent *and* connected to the surrounding cortical bone [15]. For example, inside either of the end portions of a typical healthy femur there normally exists a formation of trabecular bone, encased by – and attached to – the cortical bone forming the exterior surface of the femur [15]. At such locations, the porous structure of the trabecular bone serves equally as an absorber of impact energy due to its elasticity [15], as in various *metabolic* functions due to its additional surface area, for example in the exchange of calcium ions [17]. (Figure 1.1)

Aside from these locations, a three-dimensional network of trabecular bone most notably forms – as an intermediate stage – when the bone tries to *heal* itself as a result of fracture [19]. Whenever a severe fracture in a bone occurs, i.e. the compact cortical
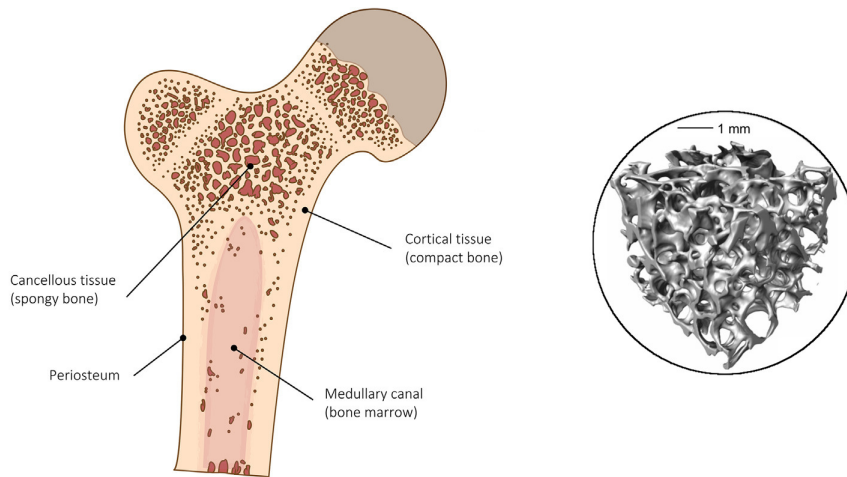
Figure 1.1: At left, an illustration of a cross-sectional view at the end portion of a femur, indicating cortical tissue (*compact bone*) and cancellous, i.e. trabecular tissue (*spongy bone*) formations. Bioactive glass is not indicated in this figure. Image adapted from Acta Biomaterialia (*A. Wubneh, et al.*) [15]. **At right**, a cubic volume of a 3D-model – derived from µCT-measurements – exhibiting the complex structure of trabecular bone (i.e. tissue). Image extracted from Acta Biomaterialia (*J.R. Jones*) [18].

bone is fragmented into two or more separate fragments – and possibly a large number of smaller shards – an entire series of reactions is set in motion at the site of the injury [19]. This rather complicated sequence of anatomical and biochemical events consists of multiple stages and involves numerous *feedback* mechanisms, all of them aimed at *regenerating* the damaged bone back to its original state [19][20]. During this gradual process of recovery and regrowth, trabecular bone is formed at an intermediate stage, ultimately to be *remodeled* into the type of compact cortical bone that resembles the original unfractured bone [19][20]. As the preceding stage in the process, the overall shape of the trabecular structure essentially *defines* the *volume* into which this new cortical bone is eventually formed. As a consequence, the way in which the trabecular structure grows and evolves is of utmost importance [19][20]. In case that, for example, the developing trabecular structure of bone is – for any reason – not able to reach out and close up all the *gaps* between the fragments of the original fractured cortical bone, these gaps will ultimately remain and the injury as a whole will not be properly healed [19][20].

At this intermediate stage in the process, the stage of trabecular bone formation, it is often most beneficial to make an attempt to *intervene* – if required – in the process of recovery, in order to assist and support the gradual regeneration of the bone [15]. The conventional way to accomplish this would be to try to fit the segments of bone together as accurately as possible, and thereafter prevent the segments from moving by the use of for example a cast or some other corresponding equipment [19]. However, in certain circumstances such traditional methods are not applicable, and novel methods

must be utilized.

Such circumstances arise when for example significant *defects* are present in the fracture, i.e. locations within the fracture in which large portions of the original bone are completely absent, either due to the severity of the injury itself (a portion of the bone is completely *demolished*) or as an unavoidable consequence of surgical procedures performed on the injury, although aimed at salvaging as much of the bone as possible [5]. An analogous situation is encountered when for example a surgical procedure is required to remove a *tumor* or an *infected* region from the bone [21], resulting in the creation of a similar defect between the remaining portions of healthy bone [22]. The defect in this context refers to the *absence* of bone, i.e. an opening or a cavity between the remaining segments of bone that must somehow be closed up for the healed bone to correspond – at least in its overall shape – to the original bone.

By convention, the process of fracture healing can in general be categorized into two distinct classes depending on the degree to which the fragments of bone are initially separated, i.e. the processes of *direct* or *indirect* fracture healing [20]. In direct fracture healing the separation (the gap) of the fragments of the original cortical bone are either less than 0.01mm = 10µm apart (i.e. *contact* healing) or less than 1.00mm = 1000µm apart (i.e. *gap* healing) [19]. In either case, the development of new cortical bone begins directly from the edges of the fracture in the original bone, without the intermediate stage of trabecular bone [19]. In *in*direct fracture healing, however, the separation of the fragments of the original bone is on average considerably wider, and direct growth of the original cortical bone is – for various reasons – not feasible [19]. Indirect fracture healing therefore proceeds through the intermediate stage of trabecular bone formation, during which a network of bone forms between the fragments, in order to connect them together and to eventually close up the gap entirely [19]. However, in certain instances, this process requires guidance and support in the form of a *scaffold*, i.e. an artificial or transplanted structure adjoining the edges of the cortical bone, for the trabecular bone to be able to develop properly [15].

1.2 The Role of Bioactive Glass Scaffolds

For the purpose of constructing a scaffold [15][16], there exists a number of suitable materials, some synthetic and others formed from *transplanted* tissue, either from the organism itself (*autograft*) or from another organism of the same species (*allograft*) [16]. The focus of the research on synthetic materials has in time been shifted from *inert*, unreactive materials, to materials that are biologically active, i.e. materials that mimic biological materials or that are biocompatible, and furthermore are able to *react* to the biological environment [18]. These *bioactive* materials would optimally offer a degree of

physical support and guidance to the growing trabecular structure, and simultaneously stimulate the process of bone growth by releasing (or absorbing) chemicals to (or from) the injury site [15]. In addition, it would be beneficial if the supporting structure would gradually *dissolve* into bodily fluids, in time disappearing entirely [15].

A class of materials that fulfills these criteria is the group bioactive glasses [18]. The physical structure of these materials – in the atomic level – is the amorphous structure, similar to that of regular household glass [4]. Their elemental composition also resembles that of ordinary glass, being primarily composed of a few commonly encountered elements, such as silicon Si, sodium Na, calcium Ca and phosphorus P [4]. Additionally the amorphous structure also contains substantial amounts of oxygen O [4]. The crucial factor defining the properties of these materials is the exact ratio of such elements, i.e. the fraction or percentage in which they constitute a particular type of bioactive glass [4][18].

The bioactive glass S53P4 consists of (as a percentage by *weight*) 53 wt.% SiO_2, 23 wt.% Na_2O, 20 wt.% CaO and 4 wt.% P_2O_5 [5]. For this particular composition the rate of dissolution of its constituent chemicals, especially in the specific biological environment of an injury, appears to be quite promising [5]. In addition, the S53P4 seems to also exhibit certain antibacterial properties, although its chemical composition is in itself non-toxic and as such harmless to the healing bone [23]. Thus, by inserting a supportive structure composed of this material to the injury site, specifically into the *defect* between the fragments of bone, the process of healing and regeneration of bone would – presumably – be substantially enhanced [5][24]. This, of course, is exactly the hypothesis that the research project, as a whole, is set out to verify and confirm [25].

As a subsidiary endeavour, this Thesis focuses on the determination of the three-dimensional structure of the trabecular bone that grows *in the midst of* the structure of the implanted scaffold, which in turn is formed by small individual *granules* composed of the bioactive glass S53P4, aggregated together to form a compact pellet [25]. This type of scaffold offers only a limited amount of *physical* support to the defected bone, and therefore an additional supporting structure, e.g. a metal plate, is often required to ensure the stability of the injury site [18]. The principal function of this type of scaffold is, however, to enable a sufficient amount of *chemical* interaction to take place within the scaffold by maximizing the *surface* area of the bioactive glass, as the exhange of chemicals with bodily fluids or adjacent bone formations predominantly occurs on the surfaces of the granules [5]. To these surface layers the developing trabecular bone also *attaches* itself during growth [18]. As the chemical composition of these granules is expected to change over time, it would be of vital importance to also be able to determine the *rate* of this development by estimating the amount of material (bioactive glass) that has altered its composition, i.e. its density or elemental constituents, due to

its exposure to the biological environment [18]. Fortunately, x-ray microtomography has the intrinsic capability to accomplish exactly that. Combined with the capability to determine the overall structure of a sample at the length scale of micrometres, x-ray microtomography then appears to be an optimal method for measuring these samples.
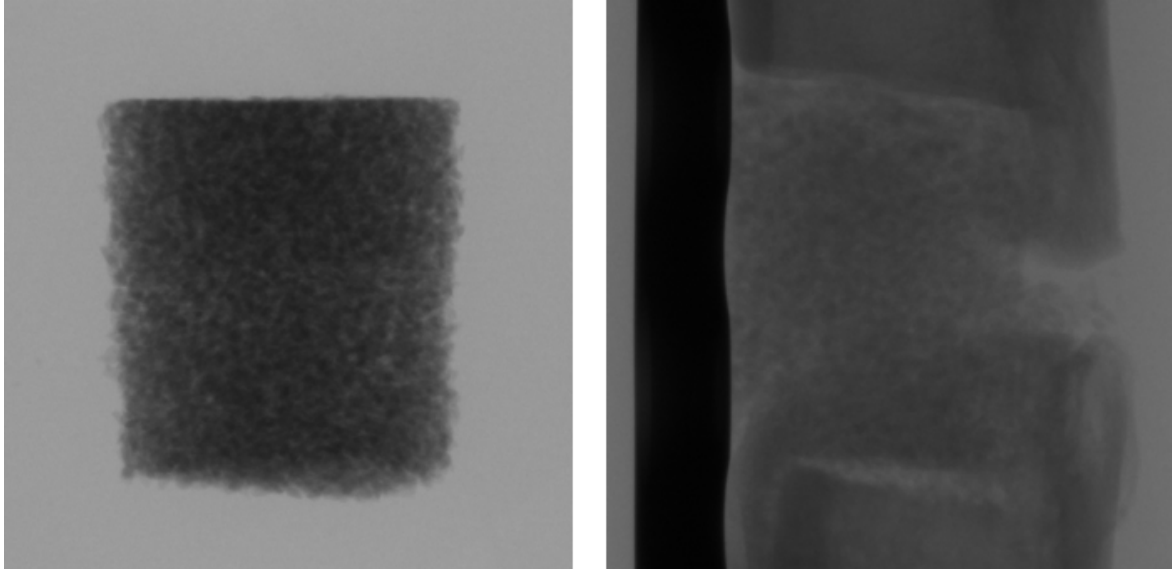
Figure 1.2: At left, a plain unused scaffold of bioactive glass S53P4. **At right**, a similar scaffold that has – previous to being harvested as a sample – been implanted into an induced defect between the two visible segments of a femur in a living rabbit. The dark rectangular region on the image at right is the supporting metal plate. Both images are the result of a separate *conventional* x-ray scan, conducted prior to the actual x-ray microtomographic measurements. The subsequent x-ray microtomographic scans and their *reconstruction* into a 3D-model enable the 3D-structures of the samples to be evaluated in detail without any *overlap* from different regions of the sample, which is clearly evident in these images (*radiographs*). Sample identifiers: image at left D112, at right D26.

1.3   X-ray Microtomography and Image Artefacts

During an x-ray (micro)tomographic scan the probed sample (*object*) is rotated in front of an x-ray source and a detector records typically a very large (~ 1000) number of *radiographs*, i.e. conventional x-ray scans (Fig. 1.2). The sample is rotated in a stepwise fashion and ordinarily one radiograph is recorded from each of the consecutive rotation angles [3]. In a *cone-beam geometry* the source can be regarded as point-like, and the x-ray radiation emanates from this point as a *cone* towards the plane of the detector, with the rotating object (sample) positioned in between [1]. In x-ray microtomography the magnification of the object is a result of this geometrical relationship between the source, the object and the detector [1]. (See illustration in Chapter 2, Figure 2.4.)

The two-dimensional (2D) radiographs are in actuality *projections* of the internal

structure of the sample onto the plane of the detector, viewed from a particular rotation angle [3]. The features, i.e. the shapes and contours, which form on the plane of the detector (the 2D-surface of an individual radiograph) depict the overall *attenuation of radiation* that the x-ray beam has undergone as it has advanced from the x-ray source, through the sample and finally onto the detector [3]. The quantitative value of an individual *pixel* on the radiograph (corresponding directly to an individual pixel on the detector) hence contains all the *cumulative* information of the attenuation of radiation in a single line – within a cone-like profile – from the source onto the detector, passing through the sample and attenuating as it encounters matter on its way [3]. As a result, the internal structure of the object, i.e. variations in density and elemental composition, may cause dense regions of the object to *overlap* with other, less attenuating regions, on the resulting radiograph [2]. It may then be demanding to interpret the overall three-dimensional shape of the object – not to mention the intricate details of its structure – from individual radiographs, even when these are obtained from varying directions.

In x-ray microtomography all of these two-dimensional radiographs are *combined* by the use of various complicated algorithms to form an essentially three-dimensional *map* or *model* of the probed object [2]. By utilizing the properties of different mathematical *transformation* and *filtering* operations, e.g. Fourier transform and its inverse, all the information contained in the (circa 1000) 2D-radiographs can be rearranged and reshaped in order to mathematically construct a 3D-model of the object [2]. In this *reconstruction* of the original radiographs and their information content, each *voxel*, i.e. three-dimensional pixel, depicts the attenuation of the x-ray radiation beam at the corresponding location of the actual object [2]. The quantitative value, i.e. the *brightness*, of an individual voxel, in combination with the knowledge of its exact coordinates, can then be utilized in subsequent *image processing* operations, in which the 3D-model (i.e. the 3D-*image*) represents the actual object in a one-to-one correspondence [2]. As the attenuation of x-ray radiation depends collaterally on the density *and* the elemental composition of the material through which the beam passes, a quantitative analysis of these properties is then possible within the precision of an individual voxel [2]. (Most of the measurements involved in this Thesis were conducted with a voxel *size* of 15µm^3, i.e. an isotropic cube of volume 15µm × 15µm × 15µm.)

However, the reconstruction does not always represent the object correctly [3]. At certain instances, the resulting 3D-image is distorted by *artefacts* that may severely degrade the overall quality of the image, especially when standard laboratory x-ray sources are used in combination with samples that contain, as a component, metal or other relatively (in relation to the overall density of the sample) dense materials [3]. These artefacts are an unfortunate consequence of the inherently imprecise and inaccurate processes that generate the x-ray radiation in a standard laboratory x-

ray source [3]. Resulting from these, the energy distribution of the x-ray radiation emanating from the source is to some extent *spread out*, i.e. a certain ratio of the produced radiation has a higher (or a lower) energy than average, which in turn will lead to the phenomenon of *beam hardening*, as the radiation advances through the object that contains relatively dense components [10]. In essence, the radiation that reaches the detector is *hardened*, i.e. the beam contains a disproportionate amount of radiation with higher energies than average, and none with lower energies [10]. Beam hardening will as a consequence affect the reconstruction process by introducing features to the resulting 3D-image that in actuality do not exist at all [10]. These features – e.g. lines, shapes and regions that are excessively bright (or dark), and in addition *overlap* other features – can however be *reduced* or compensated to allow for a comprehensive quantitative analysis of the rest of the sample [26]. As the majority of the samples did in fact contain a metal plate, the emphasis of the image processing will initially be on the reduction of the artefacts in the reconstructed 3D-images.

1.4   The Set of Samples – a Preview

The set of samples consisted of 34 samples that had been – prior to harvesting – in contact with the biological environment of a living organism, i.e. a rabbit. In addition, 3 samples that had never been subjected to any biological environment were included in the measurements for comparison. Of the 34 samples, 24 were samples which contained substantial amounts of the original femur that was still attached (screwed on) to a metal plate. This was a supportive structure that had been added to extend over the injury site in order to ensure the stability of the remaining portions of the femur. The injury in itself was a deliberately introduced *defect* (a substantial portion of the femur had been detached, i.e. cut off completely). The bioactive glass scaffold – or as in 7 of the samples a *control* implant of a similar size but composed of a biologically *in*active material: poly(methyl methacrylate), PMMA – had then been inserted into this defect. As was already evident by visual examination of some of the samples, a substantial formation of newly developed bone had then grown to the defect site, on some occasions enveloping the bioactive glass scaffold – between the segments of femur – completely. The rest 10 of the 34 samples were scaffolds that were *detached* from the defect site *before* they had been enveloped by the developing bone, and hence did not contain the metal plate or any substantial amounts of bone. As already mentioned, three of the samples (of total 37) contained only plain, unused scaffolds of three distinct varieties.

The scaffolds were cylinders approximately the size of a regular cube of sugar. The femurs, in samples that still contained any, were tubular bones of approximately the same width as the scaffolds and totalling $\sim$ 10cm in length. They were originally

cut off to be of the same length as the metal plates, to which they were attached to by 6 screws, 3 above and 3 below the defect site and the scaffold. All of the 34 samples were encased in similar plastic test tubes which were flooded with liquid to aid in their preservation. Evidently the biological portion of the samples predominantly contained bone and bioactive glass, without any substantial quantities of other types of (softer) tissues. Therefore, the energy of the radiation could be adjusted to dense objects, i.e. the cortical or trabecular bone and the granules of bioactive glass, an adjustment which also led to the metal being less of a distraction (forming less artefacts in the images).

Prior to the conduction of the actual measurements, it was already revealed that a certain portion of the samples contained a scaffold of bioactive glass S53P4 (equally referred to as BAG-S53P4), which had in addition been inserted with a layer of a well-known biodegradable (co)polymer: poly(lactic-co-glycolic acid), PLGA. The thickness of the layer of PLGA enveloping the granules of bioactive glass S53P4 was designed to be either 200µm or 600µm. These samples will hence be referred to as the S53P4-PLGA (or BAG-S53P4-PLGA) -samples.

It was also revealed, and also clearly evident by visual inspection, that the samples were harvested, i.e. removed from the animal, in three different *stages* of development. As was later clarified, these stages were – counting from the implantation of the scaffolds – 2 weeks, 4 weeks and 8 weeks. At the time of the measurements, the details of the different stages and of the types of scaffolds – and also the existence of control samples altogether – were deliberately left undefined. It was then not explicitly known which samples contained which scaffold, and for how long the development and regeneration of bone had proceeded in a particular sample. However, as the general properties of bioactive glasses are rather well-known [18], as is the overall progression of the healing process of bone [27], a qualitative evaluation – based on visual observations alone – of the samples was reasonably justified as a first step on the analysis of the 3D-images.

1.5   The Thesis and the Project in General

Evidently, the development of the samples in the three different stages (2, 4 and 8 weeks of development and bone regeneration) proceeds as to be expected (Figure 1.3), in at least majority of the samples. The trabecular bone begins to form into the injury site, initially *encircling* the entire defect in some instances, then gradually forming – in the volume between the segments of cortical bone and the scaffold – a three-dimensional network of bone that reaches out into the thin volume *between* the tiny individual granules of bioactive glass, eventually enveloping them completely in all directions.

This development is already clearly evident, in the most developed samples, by a visual inspection of any arbitrary two-dimensional, cross-sectional *slice* of the 3D-image

that is produced by the x-ray microtomography measurements. Similarly evident is the gradual development of the granules of bioactive glass, as they begin to form a thin layer or a *shell* on their surfaces, apparently consisting of a material with a different density or elemental composition as compared to the bioactive glass. This development is expected and has been verified in previous research, at least in a qualitative manner [4][17][18]. The advantage that x-ray microtomography has to offer is the possibility to perform *quantitative* analysis on the three-dimensional properties of these structures. This type of investigation, utilizing x-ray microtomography to assess and evaluate these structures in a micrometre length scale, has in fact not been previously reported [5].
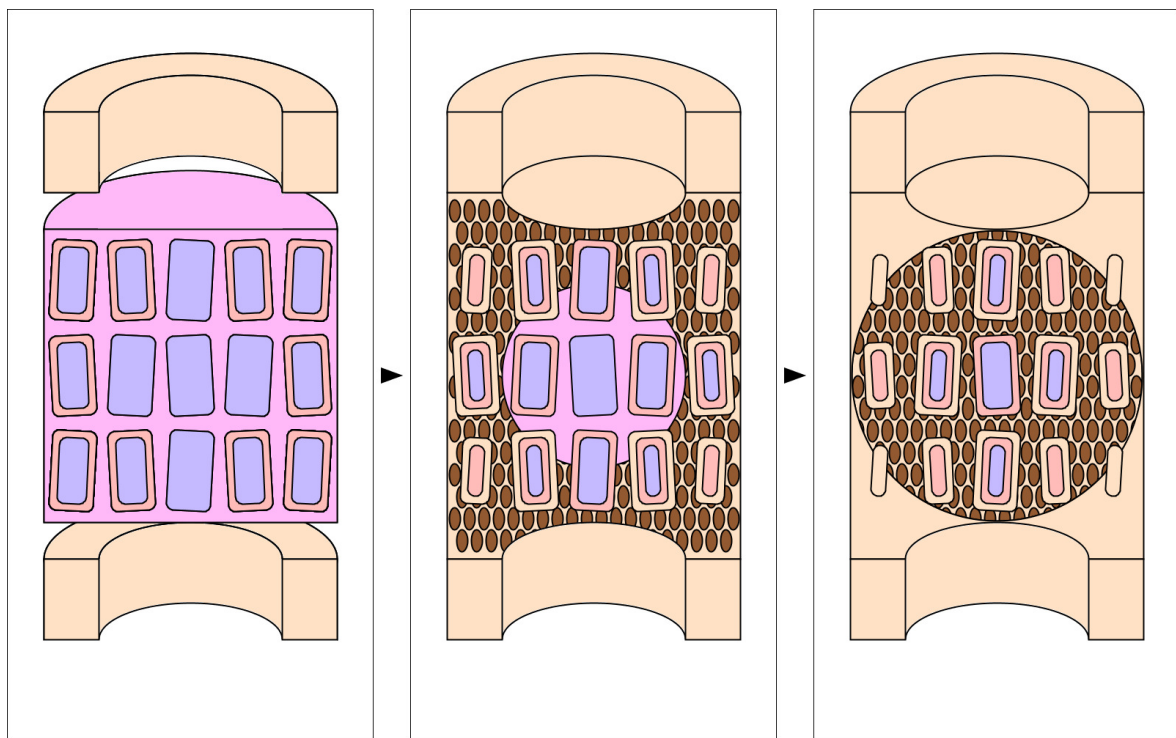
Figure 1.3: A cross-sectional *diagram* illustrating the expected development of the bone samples at a) the **Early Stage** (2 weeks), b) the **Middle Stage** (4 weeks) and c) the **Latter Stage** (8 weeks). The diagram depicts the development of the surface layers of the *granules*, a process that advances progressively from the edges of the *scaffold*, and the simultaneous formation of the trabecular bone structure, stimulated by the chemical dissolution of the granules. The trabecular structure forms into the larger volumes between the scaffold and the cortical bone, and in addition into the thin volumes *in between* the granules, promoted, and in part guided, by the gradual development of the outermost layers of the granules into a material that closely resembles natural bone. Compared to this schematic representation the actual *amount* of granules in a scaffold is around a hundred times greater and the relative *size* of the granules is on average a hundred times smaller (See Figure 1.2).

A quantitative analysis of the x-ray microtomography measurements utilizes the properties of individual voxels of the 3D-images to first of all perform a *segmentation* of the image into separate regions or volumes that are each composed of different types of materials, differing for example from their density and elemental composition, or as in

the case of trabecular bone, from their morphology [28]. The main property to analyse from the voxels is their brightness – corresponding to density and composition – and additionally for example their *connectivity* to neighboring voxels can be quantified [28].

If the segmentation can be successfully accomplished, in the next step it is then possible to determine for example the relative average densities of different materials, or as in the case of trabecular bone, their overall volume, which would otherwise be a laborious task to accomplish with any precision [7]. In addition to the volume of the trabecular bone, overall or in relation to the volume of the cortical bone, other key variables of the trabecular structure can then be determined by various algorithms, including for example the thickness and separation of the individual trabeculae on average [7][29].

The objective of this Thesis is to present a preliminary segmentation scheme in which the original cortical bone is separated from the newly formed trabecular bone, and in addition the granules of bioactive glass are classified according to the degree to which their constituents have dissolved or changed their composition. An outline of a procedure for the segmentation of the outer shells of the partially developed granules – and their separation from the adjoining trabecular structure of an almost identical brightness – is also presented. Based on these segmentations, a selection of quantitative results and a set of key variables from the trabecular structures can then be calculated.

The quantitative analysis of the 3D-images will be preceded by a thorough description of the various *image processing* methods that are utilized in the segmentation procedure. The 3D-images are initially processed by *filtering* operations to smooth out the *noise*, which is an inherent property of any images of this type. The artefacts resulting from the reconstruction process are then reduced or even removed by a novel method that combines consecutive *thresholdings* of the image with sequential *Gaussian filtering* of the resulting segmented images, followed on each consecutive step by a pairwise *subtraction* of the images from each other, the results of which are *summed* up. In the end, a *correction image* corresponding to the artefacts is formed, and as this image is in turn subtracted from the original image, the artefacts are in effect removed.

Finally, the segmentation of the trabecular and cortical bones, and the granules and their shells, is accomplished by a combination of similar thresholding procedures – including a subsequent processing of their resultant *binary* images – and additionally by the use of *morphological filtering* [28], which is a method that utilizes the differences between the shapes, forms and textures of the structures, intrinsic to both types of bone formations and the granules in general, yet similar between all the different samples.

The ultimate objective in the development of this segmentation scheme has been to ensure that the entire procedure, of all the combined image processing operations, is exactly the *same* for *every* sample, thus assuring the comparability and reproducibility

of the results. Accomplishing this would enable a quantitative analysis on the *rate* of formation of the trabecular bone, and of the simultaneous development of the granules of bioactive glass S53P4 in all *three* different *stages* of development, thus allowing for an initial assessment of the medical benefits resulting from the implantation of these types of bioactive glass scaffolds, of both S53P4 and S53P4-PLGA type.

The primary reason for the deployment of the additional PLGA-layer is a – potentially achieved – enhancement in the *inflammatory response* at the site of the injury, which could feasibly be *beneficial* to the healing process in general, provided that the magnitude of the response can be controlled [24][25]. By combining this newly acquired knowledge with the refined understanding on the behaviour of the outermost surface (*reaction*) layers of the granules during the healing and regenerative process, a valuable new insight into the optimal usage of bioactive glass for the recovery, regrowth and *remodeling* of injured bone (i.e. the regenerative process) is obtained.

Establishing all the varied mechanisms of action in the regenerative process of bone – induced by this particular type of bioactive glass, S53P4 – and assessing all the potential medical benefits resulting from the usage of the additional PLGA-layers to envelope the granules, is well beyond the scope of this Master's Thesis in Physics, but hopefully a determination of the three-dimensional structure of the newly formed bone – stimulated by the bioactive glass scaffolds throughout the gradual regenerative process – will prove to be a beneficial contribution to the Medical research project in general. As for the other main topic of this Thesis, the reduction of image artefacts caused by metal, the methods developed here could perhaps turn out to be applicable in a wide variety of circumstances, possibly even providing a viable new alternative to the various techniques that tomography laboratories already universally use.

> The outline of this Thesis will follow the outline of this introductory Chapter, which constitutes the first Part of the Thesis. The second Part, Materials and Methods, consists of two separate Chapters, X-ray Microtomography and Bioactive Glass Scaffolds, that will provide a thorough description of the theoretical background on both subjects, with a level of detail that would not be feasible in this Introduction. The third Part provides a detailed account on the actual Measurements, and the fourth Part describes the Image Processing methods and techniques in general. The final fifth Part of the Thesis contains various Appendices, detailing some of the subjects of the preceding Chapters in more depth.

Part II

Materials and Methods

2. X-ray Microtomography

X-ray microtomography is a well-established and widely utilized method of materials science for conducting measurements on the internal structure of materials in a precise and non-destructive manner [1]. The attained resolution of the technique spans the micrometre range of approximately $0.1\ldots100\mu m$ ($10^{-7}\ldots10^{-4}$m), thus making it an optimal choice for the study of materials that contain structures with dimensions in this length scale [7].

Alongside its conventional utilization in the research of materials, the method is also regularly employed by other fields of research, for example chemistry, biology and medicine [3], or any other disciple – e.g. archaeology – that may require detailed information on the exact structure of their respective objects of interest (i.e. samples) at the sub-millimetre to micrometre length scales. These objects of interest may range from novel (or age-old) materials to the inner structures of living beings, for example of minuscule samples from plant, animal or even human tissue [3][7]. The main benefit of the method for the above mentioned fields of research is the non-destructive nature of x-ray measurements, that is, the sample – once harvested – does not need to be dissected, stained or otherwise impaired prior to the measurements, and the inner structure of the sample may later be investigated in detail along any cross-sectional plane or three-dimensional region that may be required by the study in question.

X-ray microtomography (also referred to as micro-computed tomography or μCT) is in fact a variant of the more renowned and commonly utilized computed tomography method, the CT-scan, performed routinely in medical centers or hospitals [6][9]. This technique (i.e. medical *modality*) has for decades been the prime non-invasive method to scan the inner structure of human body in order to detect any injuries or other maladies in the tissues of organs without the need to perform invasive surgical procedures to the patient [6][9]. The benefits of such three-dimensional scans are obvious, however, the resolution of the scans may not always be sufficient to detect minuscule details in the sub-millimetre length scales, at least not on standard CT-equipment [3]. Therefore, on occasion, the utilization of x-ray *micro*tomography (on small samples) may be required.

The working principles – in a mathematical sense – of a CT-scan and a typical x-ray microtomography measurement are essentially the same, although the machinery

involved in the CT-scan is markedly different from a regular x-ray microtomography apparatus, in that the x-ray source and the detectors rotate *around* the measured object (i.e. the patient) in a CT-scan, whereas on a typical set-up of an x-ray microtomography measurement, the x-ray source and the detector are stationary and the measured sample rotates in between them [6]. The obtained three-dimensional images, which can be e.g. sectioned or rotated at will, are however similar and for example most image processing methods (Chapter 5) are interchangeable between these two *imaging modalities.*

The most notable difference between these two types of measurement techniques (apart from the machinery involved in the measurements) is the degree of *magnification* that a minuscule sample size enables for the x-ray microtomography measurements [1]. The scale of the CT-scan apparatus (the *gantry* [6]) must be constructed to allow for a human patient to fit in between the rapidly rotating x-ray source and detector arrays, whereas on x-ray microtomography measurements the typically inanimate sample can be positioned relatively close to the x-ray source [9]. By positioning the detector at a relatively large distance away from the sample and the source, the magnification can hence be increased several times as compared to a CT-scan [1].

On both of the measurement methods a very large number, typically circa 1000, *conventional* x-ray scans are first performed on the object that rotates in relation to the x-ray source and the detector (or an array of detectors for a CT-scan) [6]. These *projection* images are then combined by advanced mathematical algorithms to form a three-dimensional *reconstruction* of the measured object, which for a regular CT-scan is typically a human patient [6][9].

The reconstructed 3D-image has the same magnification as the projection images of the conventional x-ray scans, and their resolution is also in a sense proportional to the projection images. However, whereas on the 2D-images the smallest element in the image is a – typically square or rectangular – *pixel*, on the reconstructed 3D-images the smallest element in the image is a – typically cubic – *voxel* with similar dimensions as those of the pixel, but in three dimensions [6]. Similar to the 2D pixels, each cubic voxel has an intrinsic brightness that depicts the measure in which the x-ray radiation has *attenuated* at the corresponding location within the sample [6]. Therefore, the value of the brightness (often visualized in a *Gray Value* -scale [30]) corresponds directly to the density and elemental composition of the measured object at the location of the voxel, as these two quantities collaterally determine the amount of attenuation that a beam of x-ray radiation undergoes as it passes through the measured object [6].

The reconstruction can be performed by various different algorithms or corresponding mathematical procedures, but on this Thesis the focus will be on the renowned and indeed archetypical Filtered Back-Projection -algorithm, which was one of the first algorithms developed for tomographic reconstructions and is still widely deployed on

standard µCT- and CT-equipment [9]. The algorithm has an elegantly simple internal structure which can be implemented with ease and is simultaneously efficient and robust [10]. An *optimized* variant of the algorithm was also preinstalled on the x-ray microtomography equipment that was used for the measurements in this Thesis, and consequently all the reconstructions were carried out with it (Subsection 4.2.2).

The Filtered Back-Projection -algorithm, although one of the most widely utilized reconstruction methods [11], has certain inherent limitations and deficiencies that may cause the algorithm to produce excessive amounts of brightness on the reconstructed images, particularly on samples that include materials which are relatively dense and contain heavy elements, most often metals [11]. These *metal artefacts* manifest themselves as regions of excessive brightness that appear to *emanate* from the metal on the reconstructed images, thereby effectively *smearing* the areas of the image that are in the closest proximity to the metal [11]. This naturally has a detrimental effect on the overall quality of the image and may cause the subsequent analysis of the image to be altogether unfeasible. However, a *reduction* of the metal artefacts is achievable by a combination of various image processing methods, even to a degree that the artefacts are in effect *removed*, both for which novel methods will be presented in Chapter 5.

In this Chapter 2, the mechanisms underlying the emergence of the metal artefacts, and also other image artefacts of varying origin, are described in Section 2.4. Preceding this in Section 2.3 is an outline of the tomographic reconstruction procedure involving the Filtered Back-Projection -algorithm. Preceding both of these Sections is a general description of the fundamental properties of x-ray radiation – and its typical production using standard x-ray tubes – in Section 2.1, followed by a brief characterization of the attenuation properties of x-ray radiation in Section 2.2.

2.1   X-ray Radiation

X-rays are an energetic form of electromagnetic radiation with a wavelength λ that corresponds to the natural length scale of atoms constituting matter [6]. Due to the intrinsic energy of the radiation, x-rays are able to penetrate matter efficiently, allowing for the *imaging* of the inner structure of the probed object [6].

In general, x-ray radiation can be categorized as *soft x-rays*, with wavelengths λ in the range $1 \cdot 10^{-9} \ldots 1 \cdot 10^{-10}$m, corresponding to an energy range of $1.2 \ldots 12.0$keV, and as *hard x-rays* with wavelengths λ in the range $1 \cdot 10^{-10} \ldots 1 \cdot 10^{-11}$m, that correspond to energies in the range $12.0 \ldots 120.0$keV. In this Thesis, the energy of x-ray radiation was 80keV in all measurements that were performed on the samples (See Chapter 4).

X-ray radiation originates from the inner electron shells of atoms, and due to the tightly bound nature of these electrons, the energy needed to produce x-rays is

considerable [6]. Concomitantly, the energy that is transferred to the *detector* – and the sample – during the imaging is substantial [6]. Therefore, a number of precautions should always be taken prior to conducting x-ray measurements [6].

2.1.1   The Electronic Structure of Atoms

The congregation of electrons that envelop the *nucleus* of an atom arrange themselves into discrete *electron shells* that are separated from the next by a difference in their innate binding energies [6]. Each shell may be occupied by a pre-determined number of electrons only, determined by the rules of quantum mechanics [6]. The total number of electrons in an atom corresponds to the number of *protons* in the nucleus, although *ionization* may temporarily affect the number by a removal or an addition of typically one or two electrons from the *outer* shells of the atom, often resulting in an emitted *photon* with energies that range from the infrared to the ultraviolet spectrum of radiation [6]. The electrons of the *inner* shells, however, are typically very tightly bound to the nucleus, and – for the heavier elements – require a formidable amount of energy to be removed [6]. However, when the requirements for the energy are met, a cascade of events within the atom will in the end produce x-ray radiation that may then be utilized in, for example, imaging or other types of x-ray measurements [6].

In a similar way that x-ray radiation is produced by the utilization of the inner shell electrons, the same electrons are also employed for the *detection* of x-ray photons, and indeed the entire process comprising an x-ray radiation measurement is based on the interaction of the photons with atoms that constitute the matter from which the measured *sample* is composed of [6].

2.1.2   Radiative Transitions and Deceleration Radiation

The rules of quantum mechanics determine the levels of energy in the electron shells of an atom [6]. For this reason, most events within the electron shells, for example the *transitions* of electrons from one shell or energy level to another, require a definite pre-determined energy and have a well-defined *probability* of occuring [6]. This energy may be transferred to the atoms constituting the matter by for example radiation from some external source or fast-moving electrons entering the matter [6]. By interacting with the inner electron shells, the radiation or external electrons may then cause some of the original electrons to be removed from their initial positions within an atom [6].

The removal of an electron from the inner shells of an atom will initiate a cascade of events within the atom that eventually leads to a high-energy (x-ray) photon being emitted from the atom [6]. This photon will have a distinct wavelength – and energy due to the interconnectedness of these quantities – and it is therefore referred to as a

characteristic x-ray [6]. Every element produces these characteristic x-rays in different energies due to the subtle differences in the structures of their electron shells [6]. This property, i.e. *coherence*, can be utilized in certain measurement techniques, however, in a standard laboratory x-ray source, a substantial portion of the radiation is *incoherent* due to the mechanism that produces it, namely *deceleration radiation* [6].

As a fast-moving electron approaches the inner electron shells near the nucleus of an atom, it will be decelerated by the similar *charges* of the tightly bound inner-shell electrons already occupying the area [6]. This causes the approaching electron to alter its trajectory, which in turn leads to the emission of photons that, due to the kinetic energy of the electron, are in the x-ray range of the electromagnetic spectrum [6]. The initally fast-moving electron is gradually decelerated as it encounters more atoms in the matter it passes, and hence the wavelength and the energy of the produced radiation does not have a distinct energy, but a wide distribution of decreasing energies instead [6]. A large number of such electrons will then produce a *continuous* spectrum of x-ray radiation [6].

Similar processes involving the *radiative transitions* of inner shell electrons, that cause the emission of the characteristic x-rays – initiated here by the external *electron beam* – are also responsible for the subsequent attenuation of x-ray radiation when it in turn encounters matter (Section 2.2).

2.1.3   Production of Radiation in X-ray Tubes

A standard *x-ray tube* consists of a high-voltage vacuum tube in which electrons are accelerated to high velocities and directed to collide with a target composed typically of tungsten (W) metal [6]. The collision of the electron beam with the target material then produces x-ray radiation that is emitted through a slit or a window, typically composed of beryllium (Be) [6]. The sample to be measured is positioned in the path of the x-rays exiting the tube, and a detector records the radiation that has passed through the sample [6].

By adjusting the voltage, the maximum energy – and concomitantly the center point of the average energy – can be tuned to a preferred value [6]. By adjusting the current that controls the amount of electrons in the beam, the number of photons can be regulated [6].

The set-up is simple and elegant, however, in standard laboratory x-ray tubes the mechanism by which the radiation is produced results in a broad spectrum of x-ray radiation that may have certain detrimental repercussions on the quality of the measurements, especially if the sample contains materials that have substantially disproportionate densities or elemental compositions [6].

2.1.4 Energy Spectrum of X-ray Tubes

As the electron beam in the x-ray tube collides with the atoms of the target material, a portion of the electrons – determined by their trajectory, kinetic energy and the rules of quantum mechanics – interacts with the inner shell electrons of the atoms in a way that results in the ejection of an inner shell electron out of the atom [6]. This deficiency of an electron will however immediately be refilled by an electron from a higher shell of the same atom, that simultaneously releases the difference in the binding energies of the shells as an x-ray photon with a distinct energy and coherent wavelength [6].

This process produces characteristic x-ray radiation, resulting in high and distinct *peaks* in the spectrum of the radiation (Figure 2.1). A substantial portion of the overall spectrum is however formed by the incoherent deceleration radiation, sometimes also referred to as *Bremsstrahlung* [11]. The *mean energy* of the energy distribution, located approximately at the center of the broad main peak (disregarding the sharp peaks of the characteristic x-rays), is typically a long distance away from the maximum energy, which is determined by the peak voltage (and results from a direct hit by the colliding electron, where all kinetic energy is transferred) [10]. Therefore, a substantial portion of the x-ray photons have energies that are considerably *less* than the maximum energy.
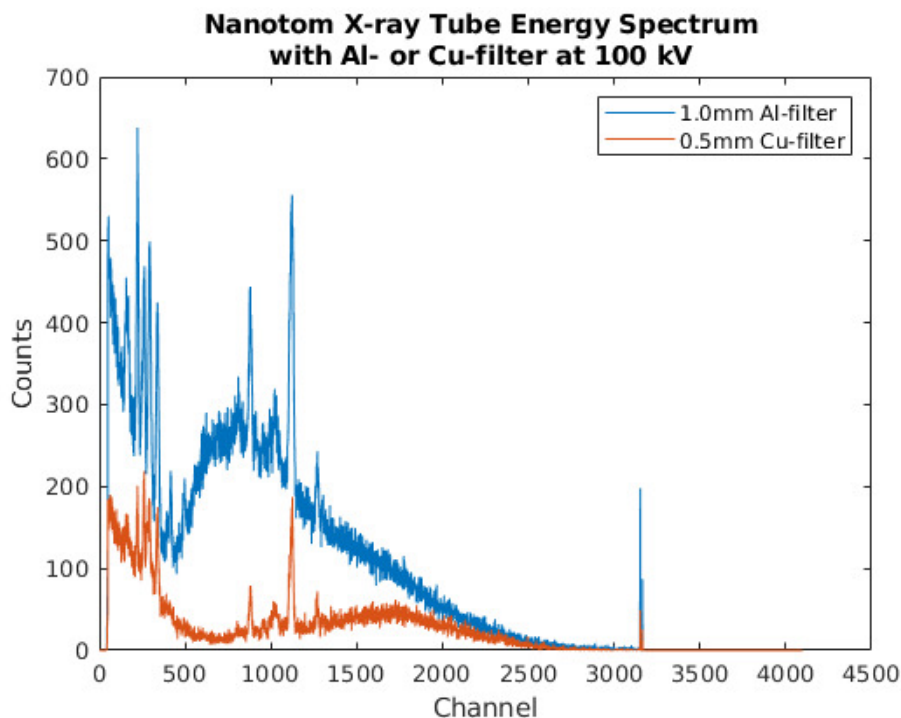
Figure 2.1: Energy spectra of the Nanotom x-ray tube at 100kV peak voltage with alternative *filters* placed in the x-ray beam. As can be clearly observed, the 0.5mm Cu-filter attenuates the radiation in the lower parts of the energy range more efficiently than the 1.0mm Al-filter (above Channel 500, data below can be ignored). Data from University of Helsinki's Laboratory of Microtomography [31].

2.1.5 X-ray Detectors and Imaging

X-ray radiation is typically measured with detectors that consist of a large array of minuscule solid-state elements which can distinguish separate x-ray photons, but are unable to discern the energies of these quanta [6]. Therefore, the quantitative value of an individual pixel in the detector measures only the intensity of the radiation that impinges on the location of the pixel [6]. The image that consequently forms on the flat panel of the detector will hence contain valuable information on the attenuation of x-ray radiation in general, but without a trace of any energy dependency of the x-ray photons that have passed through the sample [6]. If the sample for example contains dense materials or heavy elements, a portion of the x-ray beam may become hardened as it passes the sample, which may be detrimental to any potential x-ray microtomography images, since the reconstruction algorithms are often unable to function properly in these situations [11]. Due to an inconsistency in the acquired data, caused by the beam hardening phenomenon, severe image artefacts may then form to the μCT-images [11].

2.2 Attenuation of X-ray Radiation in Matter

X-ray radiation is renowned for its ability to penetrate matter efficiently and hence reveal the inner structure of, for example, the human body, in imaging modalities such as the conventional x-ray scan or the CT-scan performed in hospitals [6].

However, for the radiation to be able to reveal the inner structures of the objects it probes, there has to be a *change* in the intensity of the radiation as it passes through matter [6]. If it were not for this change, the radiation that reaches the detector would be completely unaltered from that of the source, and no information could be extracted from the scans [6].

A measure for this change in intensity is the *attenuation* of radiation [9]. In the most straighforward scenario, an object would be positioned between the source and the detector, and the change in the intensity I, as compared to the intensity I_0 of the plain source, would be measured [9]. From the ratio of natural logarithms taken from these quantities, and with a prior knowledge of the thickness L of the object, a *linear attenuation coefficient* μ can be calculated according to the *Beer–Lambert*-law [10]:

$$I = I_0 e^{-\mu \Delta x} \Rightarrow \ln(\frac{I}{I_0}) = -\int_L \mu dx \tag{2.1}$$

This equation, however, applies only to objects with a constant density and furthermore, for monochromatic radiation of a distinct energy only, and therefore can *not* be used in conjunction with a typical polychromatic laboratory source [11].

For more realistic scenarios, a more precise equation should therefore be derived,

preferentially taking into account the energy dependencies of all distinct attenuation
mechanisms of radiation, which for x-ray photons with energies in the range utilized in
this Thesis, are: *photoelectric absorption*, coherent *Rayleigh scattering* and incoherent
Compton scattering [10]. Fortunately, such an equation can be derived [32], and all
different factors affecting the attenuation of x-ray radiation can in essence be summed
up into a single quantity [32].

The quantity that incorporates the energy dependencies of different attenuation
mechanisms is the *mass attenuation* coefficient μ/ρ, which is plotted for four materials
and photon energies in the range 1keV ... 1000keV in Figure 2.2.
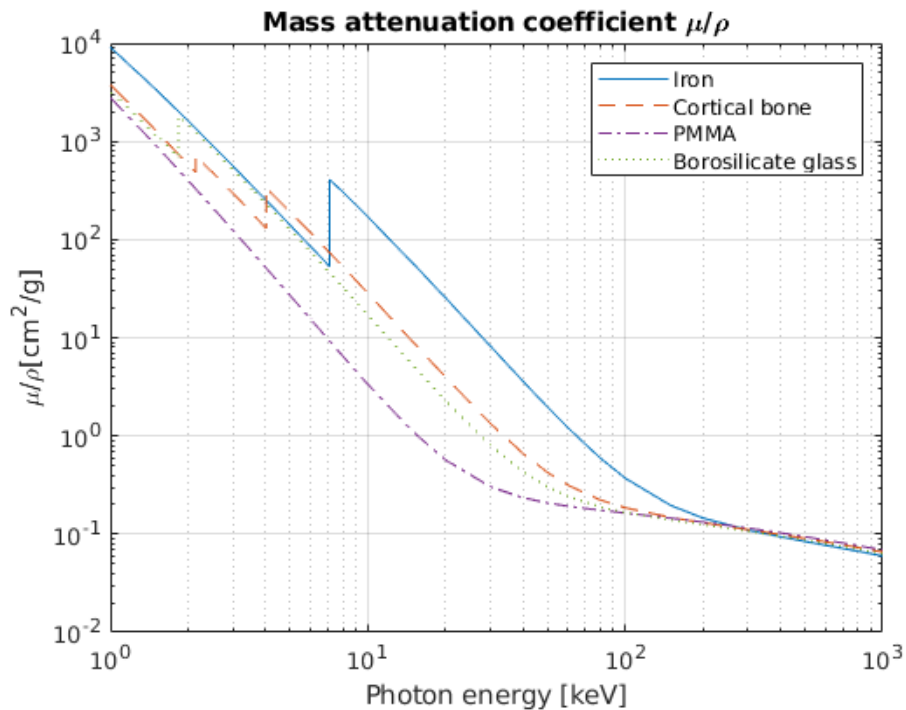
Figure 2.2: Mass attenuation coefficients μ_{en}/ρ for iron, cortical bone, PMMA and borosilicate glass.
The borosilicate glass is merely a representative example of typical values attained by silicate glasses,
and as BAG-S53P4 contains substantial amounts of heavier elements (compared to boron B) such
as Na and Ca, the curve would correspondingly be higher. Data from NIST (National Institute of
Standards and Technology) [32].

As can be seen from the Figure 2.2, the four different materials – all related to
this Thesis – attenuate the radiation in a distinct pattern following a curve that for
the heavier elements contains sudden changes in their values at certain exact locations
of the curve [32]. These locations correspond to the characteristic energies of certain
elements constituting the material (Subsection 2.1.2).

2.2.1 Scattering and Absorption of Photons

In the energy range of x-ray radiation utilized in this Thesis, three principal mechanisms of interaction with atoms leading to the attenuation of the x-rays can be distinguished [6]. The three mechanisms are photoelectric absorption, coherent Rayleigh scattering and incoherent Compton scattering [6]. In addition to these three, other mechanism of interaction with atoms constituting the matter also exist for photons with considerably higher energies [6]. Of the three, the coherent scattering merely alters the trajectory of a ray of radiation, whereas the other two involve a transfer of energy between the photon and the atom [6]. The *probability* of the interaction between the photon and the matter it passes through can be described with the quantity *cross section σ*, which depends on energy and is plotted in Figure 2.3 for the element iron Fe [33].
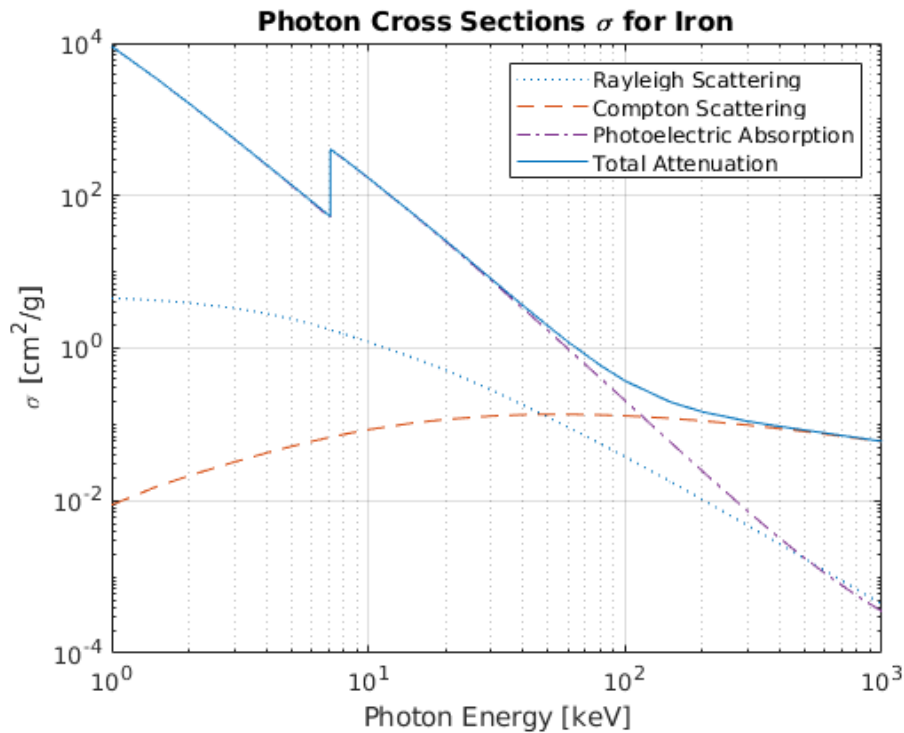
Figure 2.3: Cross sections σ for iron, the primary elemental constituent in the metal plates of the samples which were measured with a *peak* voltage of 80kV, thus creating a distribution of x-ray photons with a *maximum* energy of 80keV. Data from NIST (National Institute of Standards and Technology) [33].

A photoelectric absorption may occur – with a definite probability – when a photon encounters an atom, which in essence *absorbs* the entire photon, simultaneously ejecting one of its electrons [6]. It is the most prominent mechanism that causes the attenuation of moderate-energy x-rays in dense, heavy elements (See Figure 2.3) [6].

The coherent Rayleigh scattering is *isotropic* in a sense that the scattered photon may change its trajectory to any direction, even scatter backwards, with a probability

that does not have a significant dependency on the direction [6]. As was already mentioned, the energies of both the scattered photon and the atom as a whole remain the same [6].

An important feature of Compton scattering is the dependency of the *scattering angle* – that is, the direction to which the photon alters its trajectory – on the energy of the radiation, a property that can be described with the *Klein–Nishina formula* [11], which essentially states that as the energy of the radiation increases, the angle to which the photon is preferentially scattered decreases and approaches the initial direction, i.e. the scattering angle remains close to the initial trajectory [11].

This may be an important factor causing *variation* and a *division* into discrete components in the *scattering artefacts*, to be described in Subsection 2.4.3, although the energy of the x-ray radiation was relatively small in the measurements conducted in this Thesis.

2.2.2   Density and Elemental Composition of Matter

The three distinct attenuation mechanisms introduced in the previous Subsection differ also from the probability in which they occur in varying materials [6]. The photoelectric absorption and the coherent Rayleigh scattering both depend primarily on the elemental composition of matter, i.e. the *atomic number Z* of its constituent elements, whereas the incoherent Compton scattering depends on *electron density* of the matter, which could be relatively high in a material that contains only light elements with low Z, but is simultaneously densely packed with atoms [6].

The three attenuation mechanisms hence cause the *overall* attenuation of matter to be simultaneously dependent on the density *and* the elemental composition of the material [6]. Together with the innate energy-dependence of each separate attenuation mechanism, the resulting interconnected network of dependencies can become rather complex. This, however can be turned into an advantage, since it allows for the composition of materials to be distinguished with great precision.

2.2.3   Brightness and Contrast in X-ray Images

An x-ray detector can typically measure only the intensity of the radiation and cannot distinguish the energy of an individual photon, that is, whether its energy has altered as it has passed through the sample [6]. The intensity of the radiation, however, does contain information on the attenuation of the radiation, and this can be utilized, in the end, to determine the brightness of an individual voxel in the reconstructed 3D-image [6]. Due to the collateral dependency on the density and the elemental composition of the attenuation mechanisms, the brightness and contrast of a voxel hence depict both.

2.3 Tomographic Reconstruction

As the working principle of tomography has already been outlined – in a qualitative manner – in the Introduction (1.3) and at the beginning of this Chapter, this Section focuses on describing the mathematics of the procedure in a brief and compact form, as presented by Hsieh [10].

This textbook example involves only two-dimensional projections, and is hence not directly comparable with the optimized Feldkamp-algorithm [11] for 3D cone-beam geometry that was used in the reconstructions of this Thesis, but due to the complexity of the algorithm – and of the 3D geometry in general – a 2D example is presented here. Figure 2.4 illustrates a 3D cone-beam set-up, from which 2D flat-panel projections are obtained. The procedure presented by Hsieh [10] involves a 2D-projection, which can be visualized as a separate *fan* of an infinitesimal thickness in the cone formed by the x-ray beam. In this Section though, this fan of x-rays is further reduced to an even simpler form, and only *parallel beam* geometry is employed (Figure 2.5).

Since the Feldkamp-algorithm is in the end based on the same principle of Filtered Back-Projection as the procedure presented here, the potential artefacts resulting from its use are similar in their form and overall nature (Section 2.4).
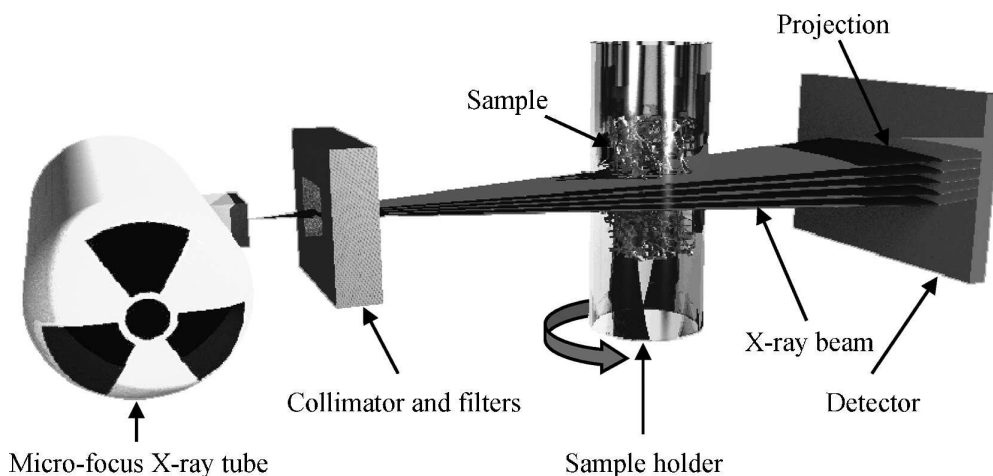
Figure 2.4: An illustration of a typical x-ray microtomography measurement set-up, including the x-ray source, the detector and a rotating sample-holder. Image from Bouxsein *et al.* [7] (Originally from [34]).

2.3.1 Line Integrals and Projections

The procedure presented by Hsieh [10] relies on the 2D-projections of an *object function* $f(x,y)$, that represents the sample (to be measured) in a parallel beam geometry, and most notably, only a thin 2D-portion of the sample is treated at once. The projection

is in a sense *one*-dimensional in this arrangement, since it only contains the values for the *attenuation* of the rays passing through the sample. The attenuation in a single line of rays can be expressed, using the *Beer–Lambert*-law [10] derived earlier, as:

$$p = -\ln(\frac{I}{I_0}) = \int_L \mu dx, \tag{2.2}$$

in which the term p is referred to as the *projection measurement*, and it is in essence a *line integral* that collects the cumulative information of the attenuation of x-rays in a single line. A collection of these line integrals then forms a single *projection* $L_z^i(x', \theta_i)$ from an individual rotation angle θ_i, which typically advances a full 360° (Figure 2.5). In an equivalent notation, the function $L_z(x', \theta)$ [2] can be expressed as $p(t, \theta)$ [10].
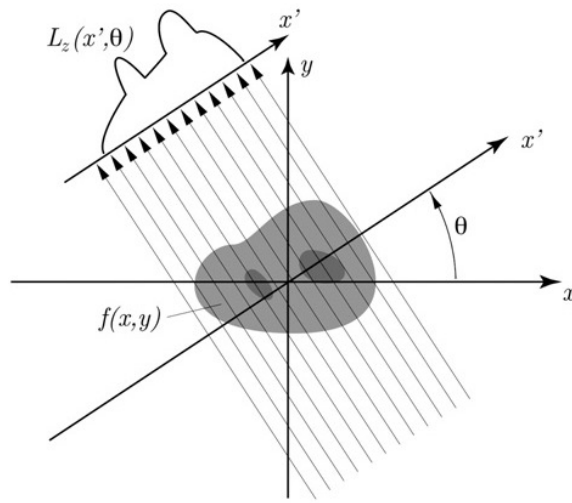
Figure 2.5: A figure depicting (parallel) lines of an x-ray beam and an *object*, represented by a (spatial) function of x-ray attenuation, $f(x, y)$. Projection $L_z(x', \theta)$ is measured from all rotation angles θ. (The function $L_z(x', \theta)$ can equivalently be expressed as $p(t, \theta)$ [10].) Image extracted from Landis *et al.* [2].

2.3.2   The Fourier Slice Theorem

The collection of projections $p(t, \theta)$ (i.e. $L_z(x', \theta)$ in Figure 2.5) does not yet represent the two-dimensional structure of the object directly, or in a more intuitive manner, and further processing needs to be done to accomplish this [10]. For this purpose, *Fourier transform* and its inverse are utilized, which in two dimensions take the form:

$$F(u, v) = \int_{-\infty}^{\infty} \int_{-\infty}^{\infty} f(x, y) e^{-i2\pi(ux+vy)} dx dy, \tag{2.3}$$

for the regular 2D Fourier transform, and for its inverse:

$$f(x, y) = \int_{-\infty}^{\infty} \int_{-\infty}^{\infty} F(u, v) e^{i2\pi(ux+vy)} du dv. \tag{2.4}$$

As the next step in the process to briefly demonstrate the working principle of a tomographic reconstruction by the Filtered Back-Projection -algorithm in a reduced 2D parallel beam geometry, the projections $p(t, \theta)$ obtained earlier are transformed to their Fourier counterparts by first performing a coordinate rotation for the initial *object* function $f(x, y) \rightarrow f'(t, s)$ [10], where

$$\begin{cases} t = x \cos \theta + y \sin \theta \\ s = -x \sin \theta + y \cos \theta. \end{cases}$$

In the new coordinate system, which relates to the coordinates of Figure 2.5 as $t = x'$, the relation

$$p(t, \theta) = \int_{-\infty}^{\infty} f'(t, s) ds, \tag{2.5}$$

holds. By indicating the Fourier transform of $p(t, \theta)$ over the variable t [10] as $P(\omega, \theta)$, the next equation is formed:

$$P(\omega, \theta) = \int_{-\infty}^{\infty} \int_{-\infty}^{\infty} f'(t, s) ds e^{-i2\pi\omega t} dt. \tag{2.6}$$

On the next step of the process, by performing a coordinate change on the other side of the above equation, for which the relation $dsdt = Jdxdy$ (in which J is the *Jacobian determinant*) [10] holds, the following equation is obtained:

$$P(\omega, \theta) = \int_{-\infty}^{\infty} \int_{-\infty}^{\infty} f(x, y) e^{-i2\pi\omega(x \cos \theta + y \sin \theta)} dxdy. \tag{2.7}$$

Then, by comparing this equation with the Fourier transform $F(u, v)$ and setting $u = \omega \cos \theta$ and $v = \omega \sin \theta$, the following equation [10] is finally attained:

$$F(\omega \cos \theta, \omega \sin \theta) = P(\omega, \theta). \tag{2.8}$$

The above equation states the Fourier Slice Theorem [10], according to which a 2D slice, i.e. a straight line, taken along the variable θ from the 2D Fourier transform of the object function $f(x, y)$ equals the 1D Fourier transform of the projection function $p(t, \theta)$ taken from the corresponding angle θ [10]. The implications of this statement are that it is therefore possible to obtain the original *unknown* object function $f(x, y)$ from the projections of the object, i.e. the function $p(t, \theta)$, at least in a scenario that enough projection angles θ are available and all the information can then be retrieved from the projections [10]. In reality, this is seldom the case, and further processing is required. For this purpose, the Filtered Back-Projection -algorithm is often utilized.

2.3.3   Filtered Back-Projection -Algorithm

According to the Fourier Slice Theorem presented in the previous Subsection 2.3.2, the projection functions $p(t, \theta)$ – which incorporate the information of individual line

integrals along *ray paths* in parallel beam geometry – correspond to straight lines (passing the *origin*) tilted at an angle θ in a 2D Fourier space with a coordinate system $(\omega \cos \theta, \omega \sin \theta)$ [10].

By collecting a large number of the functions $p(t, \theta)$, which in fact are the results of individual measurements (from an angle θ) of the attenuation of x-rays in the parallel beam geometry, it is then possible to – in essence – *fill* the corresponding 2D Fourier space with separate lines passing through the origin [10]. As the *inverse* 2D Fourier *transform* is straightforward to perform once the 2D Fourier space is filled with these lines, the sought after *object* function $f(x, y)$ can then be retrieved [10].

However, in reality the procedure is made more difficult by the practical details in the implementation of the coordinate changes [10], and the fact that the *amount* of projections is always limited [10]. Therefore, the information contained in the projections $p(t, \theta)$, that is in a sense *transferred* to the 2D Fourier space, needs to be *filtered* before it is transferred *back* into the regular space of $f(x, y)$ [10]. The filtering may, however, add too much weight to the higher (spatial) frequencies due to disparities in the sampling process, and therefore, the procedure is also prone to introduce *artefacts* into the resulting object function, which in the case of 3D cone-beam geometry is the 3D-image obtained from the x-ray microtomography measurements [10].

2.4   Artefacts in X-ray Microtomography Images

There exists many different types of artefacts that can form on x-ray microtomography images, and concomitantly, there are at least as many *causes* for the artefacts [10][11].

Some artefacts are caused by the measurement equipment itself, and others by, for example, the *motion* of the sample during the measurements [10]. Typical artefact of this type is a *ring* artefact caused by a faulty detector element [10]. These types of artefacts are often possible to avoid by, for example, repeating the measurements [10].

However, the artefacts plaguing the images presented in this Thesis are in a sense unavoidable, since they are caused by the subject of the measurements itself, that is, the metal parts included in the samples as a supporting structure for the bone. These metal parts afflict the images by introducing *streaks* of excessive brightness connecting separate portions of the metal, or by *distorting* the edge areas near the metal. The most dire artefacts, in terms of the image quality, are however the artefacts *emanating* from the metal as a region of gradually diminishing excessive brightness, and the *cupping-effect* forming within the dense material, of which the latter also forms on the edges of the dense glass scaffolds.

Therefore, the metal artefacts in actuality consist of multiple types of different artefacts, formed by distinct mechanisms and incorporated into one. In the following,

three principal mechanisms causing the artefacts are presented. The common factor in these three mechanisms, and indeed in most artefacts on µCT-images, is a critical *inconsistency* in the projection data, that is, in the projection functions $p(t, \theta)$ taken at different angles θ. This inconsistency then manifests itself into various distortions and excessive brightness in the images formed by the Filtered Back-Projection -algorithm.

2.4.1 Partial Volume Effect and Photon Starvation

The partial volume artefact appears as a distortion on the image that spreads from the edges of dense, bright objects, especially when the difference in brightness to adjacent objects – for example an object with a lesser density – or the background is substantial [11]. Often the straight edges of the dense object, for example the metal plate, appear to continue into the surrounding region [11].

On occasion, a dense object completely obstructs the path of the photons that have an insufficient energy to penetrate it, and *photon starvation* results [10][11].

2.4.2 Beam Hardening Artefacts

The beam hardening artefact often takes the form of an excessively bright *rim* encircling the edges of dense objects on the image, referred to as the *cupping-effect*, although the phenomenon of beam hardening is responsible for certain other types of artefacts as well [10][11]. In the transverse cross-sections of the metal plate these artefacts are especially pronounced. The initial cause of the phenomenon is the nature of the energy spectrum of x-ray tubes, which results in the attenuation of low-energy photons while the high-energy photons penetrate the material, and an inconsistency in the measurement data ensues as the sample is rotated and the orientation of the dense objects alter [11].

2.4.3 Scattering Artefacts

The scattering artefacts are, as the name implies, caused by the scattering of photons from the dense materials of the sample [10][11]. Although scattering as a phenomenon is responsible for much of the overall attenuation of radiation, the artefacts caused by scattering, which appear as a gradually receding region of excessive brightness emanating from the dense objects, are in part caused by *secondary photons* that have altered their trajectory inside the sample and eventually impinge on the detector at locations far from their initial path [10][11]. This creates a *zone* of inconsistent measurement data on the projections, i.e. the conventional x-ray scans (the radiographs), that during the reconstruction process then turns into the artefact on the resulting 3D-image.

3. Bioactive Glass Scaffolds

Bioactive glasses are a specific *group* of synthetic amorphous materials that comprises a small number of distinct chemical compositions, all of them intentionally developed for medical purposes during the past five decades [18]. In contrast to most synthetic glass-like materials, which are typically relatively *inert* when in contact with a biological environment, bioactive glasses possess – mainly via their dissolution products – a unique capability to *actively* enhance, promote and stimulate the biological healing process of injured tissue, primarily the recovery, regrowth and remodeling (i.e. the *regeneration*) of *bone tissue* [35]. As a *material*, bone tissue can be considered to be a *nanocomposite*, which at the level of cellular length scales consists of hydroxyapatite mineral embedded in a matrix of collagen fibrils [18]. Subsequently at the micrometre-to-millimetre length scales this material then forms a *microstructure* with either a relatively uniform *cortical*, or an intricately interconnected *trabecular* growth pattern [7].

Although the natural regenerative process of bone is on average highly efficient, on occasion it nevertheless fails to accomplish its primary function, the (re)generation of newly grown bone tissue that fully resembles the original, uninjured bone [27]. For the regeneration of bone tissue to proceed with success, an artificial *scaffold* – implanted at the site of the injury – is sometimes required, particularly at locations in which the bone contains significant *defects*, that is, sites or volumes within the structure of the bone (as an organ) in which the bone tissue is for some reason completely *absent*, as a result of, for example, a physical trauma (i.e. a severe fracture) or a surgical procedure that has been performed to remove sites of infected or tumorous bone tissue [17].

Scaffolds constructed from *bioactive glasses* are in essence supportive structures implanted to the site of the defect, designed to physically support and *guide* the newly grown bone tissue – which in due course forms into the defect – while simultaneously releasing beneficial chemicals into the injury site [17]. Surfaces of bioactive glass within the structure of the scaffold offer suitable platforms, and a porous framework, for the newly grown bone to attach itself onto and *bond* with, facilitating mechanical support and also providing guidance for the bone to progressively grow in a preferred direction [17]. The chemicals released via the dissolution of the glass promote the regenerative process of bone, both directly by stimulating the formation of new bone tissue [18], and

indirectly by allowing for the formation of additional *reaction* layers on the surfaces of the glass, which then enable the bonding to bone tissue [4]. In addition, the dissolved chemicals are beneficial to the healing process via their antibacterial properties [23].

As the dissolution process of the bioactive glass and the simultaneous regeneration of bone tissue proceeds, the newly grown bone eventually envelopes the scaffold entirely, and gradually the glass scaffold should be *degraded* completely [18]. Optimally, the rate of degradation of the glass would correspond to the rate of formation of the bone [18], but in practice there may be an inherent disparity between the rates. An alternative technique to enhance the rate of regeneration would be the insertion of a biodegradable polymer coating on the bioactive glass. The coating would feasibly stimulate the initial *inflammatory response* at the injury site, allowing for the recovery, repair (i.e. regrowth) and the ultimate remodeling of bone to proceed in a more regulated manner.

Bioactive glass scaffolds are typically assembled from a large number of small granules that together form a compact pellet, to be inserted into the defect [18]. The usage of granules increases the total surface area of the scaffold, thereby enhancing the dissolution of the glass, as the dissolution primarily occurs on a thin layer close to the surface of the material [18]. Granules also offer more surfaces for the newly grown bone to attach itself onto. For many potential applications, a uniform yet porous structure would be more optimal, but an inherent tendency to crystallize when *sintered* prevents the processing of bioactive glass scaffolds into more complex shapes and forms [18].

Scaffolds can in principle be fashioned into various shapes and forms depending on their intended usage, and in general, a scaffold can be constructed from numerous different materials, for example glasses, ceramics, polymers or metals, and can also be assembled from a combination of them, forming a *composite* structure which aims to incorporate the desired properties from each type of material it is composed of [35]. These different types of scaffold materials can either be relatively inert when in contact with a biological environment, or they can be biologically active to a varying degree, depending again on their intended usage or area of application, although other synthetic materials are seldom as intrinsically well tailored to the task of bone regeneration as the scaffolds of bioactive glasses are [35].

The main application – i.e. the primary *indication* – of bioactive glass scaffolds in the field of regenerative medicine is their usage as a substitute material for autologous bone grafts, utilized in the *two-phase induced-membrane technique*, a surgical method that relies on a mixture of coagulated blood and – in effect pulverized – bone tissue transplanted from the organism itself, to enhance the regeneration of bone tissue in sites of defects [36]. Autologous bone graft (i.e. *autograft*) is renowned for its capability to enhance the regeneration of defected bone, but limited in its availability due to the scarcity of potential donor sites in the organism. Therefore, an artificial scaffold

constructed of a synthetic, yet biologically active (i.e. bioactive) material with similar, though perhaps not comparable, properties would be an optimal solution, also reducing the amount of surgical procedures required in the induced-membrane technique.

In this chapter, the quintessential amorphous atomic structure of bioactive glasses is described, followed by a description of their chemical dissolution (and precipitation) properties. The dissolution behaviour of the glass – in itself directly dependent on the composition of the glass – produce the beneficial biological and medical properties of the material, which are detailed in the following section. Finally some examples of the main medical applications, i.e. the primary indications, of the bioactive glass scaffolds are described. Many of the properties described throughout this chapter are common to all types of bioactive glasses, and the unique properties of the composition S53P4 are emphasized only when necessary to discern it from other types of bioactive glass, for example the original bioactive glass composition 45S5, the subject of next section.

3.1 Bioactive Glass – a Brief History

The development of bioactive glasses began in the latter decades of the previous century, initially by Dr. Larry Hench who discovered the composition 45S5 in 1969, as he was searching for an alternative to the scaffold materials utilized at the time [37]. Until the pioneering work by Dr. Hench, the intended mode of operation for the supportive structure, the scaffold, was to be as biologically inert as possible, conceivably allowing for the tissue to regenerate in a straightforward and unobstructed manner [37]. This, however, was *not* an optimal approach for the regeneration of defect sites in bone and most often led to the entire injury site being enveloped in a fibrous formation consisting of cartilage that resembled scar tissue, suspending the natural regenerative process of the actual bone altogether.

Having a previous expertice on the research of glasses, Dr. Hench realized that the composition of a variety of amorphous glasses, similar to that of regular household glass, contained many elements that were not only non-toxic to the human body, but actually beneficial to the healing process when dissolved into the site of a defect in bone tissue [35]. As the research continued, it was discovered that the dissolution products enabled the formation of a layer of hydroxycarbonate apatite (HCA) onto the surface of the glass, which in turn allowed the newly grown bone to attach itself firmly to the layer, as the molecular structure of HCA closely resembles that of plain hydroxyapatite (HA), which is the natural ingredient of bone, in addition to collagen fibrils [18]. The composition 45S5 (45 wt.% silicon SiO_2 and 6 wt.% phosphorus P_2O_5) initially developed by Dr. Hench was later trademarked as BioGlass® by the University of Florida and subsequently marketed by e.g. the company NovaBone [18][35].

The limitations of the initial composition were later amended by the development of new types of bioactive glasses, among which one of the most notable is the type and composition S53P4 (53 wt.% silicon SiO_2 and 4 wt.% phosphorus P_2O_5) developed and marketed by the company BonAlive from Turku, Finland [18]. This composition not only fulfills the primary criteria, originally proposed by Dr. Hench, of bioactive glasses and the scaffolds constructed from them [18], that is, the existence of *osteoconductivity*, i.e. the ability of the glass to offer surfaces for the bone to grow onto, *osteostimulation* or *osteogenesis*, i.e. the stimulation of bone growth by the release of beneficial dissolution products, and *biodegradability*, i.e. the eventual complete dissolution of the scaffold in ideal conditions, but S53P4 also has the intrinsic capability to be *antibacterial* due to its composition and the resulting unique dissolution properties [23].

The S53P4 does not, however, have the capability to offer actual physical support for the healing bone, since it shares the same shortcoming as the original 45S5 in that it crystallizes easily when processed, i.e. sintered, into complex shapes, for example into porous yet uniformly connected structures of significant proportions [18]. For this reason the utilization of separate granules of amorphous glass to construct the scaffold is a necessity that in practice cannot be avoided, since the dissolution of the constituent chemicals primarily occurs in the *amorphous phase* of the material [4].

The dissolution behaviour and other chemical properties of bioactive glasses, as well as their latent tendency to crystallize, depends directly on the *atomic structure* that the material has – at given conditions – adopted [4], detailed in next section.

3.2 Atomic Structure of Bioactive Glass

A property shared by all different compositions of bioactive glasses is their dissolution behaviour, which is a direct result of their structure at the atomic level [4]. Although regular household glass also has an amorphous structure at the atomic level, it does not readily dissolve into water or bodily fluids [4]. The bioactive glasses, however, dissolve eagerly and continue dissolving until the entire structure has degraded completely [4]. This is due to a subtle difference in their composition as compared to regular glass, a difference that has a direct effect on the overall atomic structure – in the amorphous phase – and consequently the ability of water molecules, abundant in bodily fluids, to diffuse into the structure and instigate the dissolution of its constituent elements [4].

Along the biomedical aspects of the dissolution properties, the composition and the atomic structure of the glass are of utmost importance in this Thesis, because the precise elemental composition and the resulting atomic structure also define the *density* of the material, which – collaterally with the *effective atomic number* of the material – affects the attenuation of x-ray radiation and therefore the obtained *contrast* in the

x-ray microtomography images [6].

By itself, x-ray microtomography is insufficient to determine the atomic structure of a given material as it lacks the required sub-*nano*metre precision, and instead the utilization of, for example, x-ray *diffraction* or *simulations* of molecular dynamics are needed to resolve the exact structure of bioactive glass at the sub-nanometre ($< 10^{-9}$m) atomic length scale [4]. In numerous studies conducted with such methods, the atomic structure of bioactive glass – in general – has been resolved with great precision and a satisfactory confidence [4]. Nevertheless, some aspects of the structure still remain unresolved, and as a consequence, certain mechanisms involved in, for example, the *dynamics* of the dissolution process are yet to be determined with certainty [4].

However, the basic atomic structure of amorphous *silicate glasses*, which consist primarily of silicon (Si) and oxygen (O), and similar glasses with additional ingredients (e.g. Na, Ca or P to replace a portion of the silicon atoms), is well understood, as are the fundamental principles of the dissolution and precipitation processes of chemicals into – and from – the surrounding fluids that are in contact with these materials [4].

3.2.1   The Amorphous Atomic Structure

The type of atomic structure that bioactive glasses spontaneously tend to adopt is the *amorphous* structure characteristic to all types of glasses, an atomic structure that is in fact a quintessential *definition* of glass as a type of material [35]. An amorphous atomic structure is most often formed as a result of rapid cooling, i.e. *quenching*, of a molten, liquid phase of the material [37]. Consequently, the atomic structure of the amorphous phase resembles – at least to a certain degree – that of the liquid, molten phase, in that it does not have any definite long-range order [35].

In contrast to a *crystalline* atomic structure, in which all the constituent atoms are arrayed in a regular grid, i.e. a self-repeating three-dimensional pattern, with constant intervals between the consecutive *crystal planes*, the amorphous atomic structure arranges itself into a complex and irregular *network* of interconnected *chains* and *rings* of atoms, connected to their nearest neighbors by an atomic bond with characteristics that in glasses resemble a covalent bond more than an ionic bond [35]. Typically the elemental components of the material (e.g. silicon and oxygen) alternate in the chains that form the network, and a regular *repeating unit* can be distinguished, although the structure does not strictly have any long-range order beyond a few atomic radii [37].

In silicate glasses the repeating unit that acts as a *network-former* is a tetrahedron consisting of a silicon *cation* surrounded by four oxygen *anions* located at the corners of a four-sided tetrahedron [4]. Since the bond between the ions is to a certain extent covalent in character, the angles of the tetrahedra SiO_4 remain approximately constant

regardless of the surrounding atomic structure outside an individual tetrahedron [4]. (As the consecutive Si-ions in a chain of tetrahedra *share* the same oxygen-ion on one of their corners, the *actual* repeating unit in an amorphous structure is SiO_3 instead of a full tetrahedron [4].) The oxygen-ion shared by two consecutive Si-ions is called a *Bridging Oxygen (BO)*, and as it is already tightly bonded to two cations, it can be regarded as being chemically relatively inert [4]. (Figure 3.1)
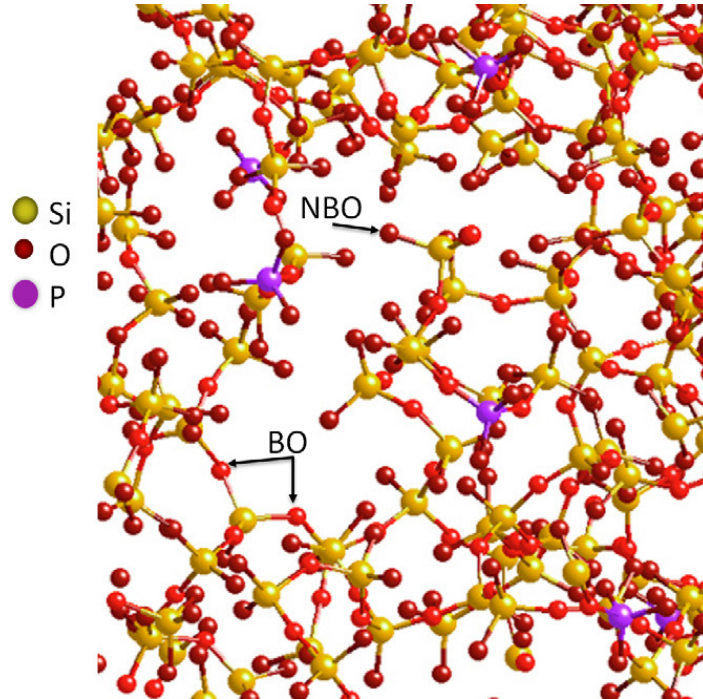
Figure 3.1: An illustration of the amorphous atomic structure of bioactive glass 45S5, a material similar in composition to S53P4. The silicon Si^{4+}-ions are indicated by yellow spheres and oxygen O^{2-}-ions by red spheres. Also indicated are purple phosphorus P^{5+}-ions dispersed among the network structure which consists mainly of silicon and oxygen ions, forming with each other atomic bonds that are primarily *covalent* and *directional* in their character. The network-forming tetrahedra SiO_4, which *share* ions on their corners with adjacent tetrahedra – although not with the similar tetrahedra formed by phosphorus – are distinguishable in the figure. The labels BO and NBO refer to Bridging Oxygen and Non-Bridging Oxygen respectively. *Not* indicated in the figure are the *network-modifier* ions, sodium Na^+ and calcium Ca^{2+}, which would be positioned within the irregular cavities formed by the randomly branching network and attached to the NBO's at the ends of individual branches with an atomic bond primarily *ionic* in character. As their name already indicates, the network-modifier ions in fact *cause* the material to adopt a more loose amorphous structure typical of bioactive glasses, instead of the more tightly bound amorphous structure of e.g. regular silicate glass. Image from Acta Biomaterialia (*J.R. Jones*) [18] (Originally from *Bio-glasses: an introduction* (*A.N. Cormack*)[38]).

The network-forming SiO_4-tetrahedra of silicate glasses, as well as corresponding tetrahedra of bioactive glasses, will form a three-dimensional network of interconnected chains, but the network is seldom *fully* connected, i.e. a certain portion of the chains will ultimately *not* be connected on both ends to adjacent chains and instead come to

an end abruptly [4]. A solitary oxygen-ion located at the end of a chain is called a
Non-Bridging Oxygen (NBO), and these ions are chemically quite active, enabling the
network to accommodate additional ions within its structure [4]. These additional ions
are typically alkali or alkaline earth metals, e.g. sodium Na^+ or calcium Ca^{2+}, and they
are generally referred to as *network-modifiers*, as their presence alters the orientation
and connectedness of the chains of SiO_4-tetrahedra [4]. The network formed by the
chains of SiO_4-tetrahedra is typically more sparse (i.e. contains more voids or cavities in
between the chains) when these network-modifier ions are introduced to the elemental
composition of the material, and in addition the quantity *network connectivity NC_{Si}*
(to be defined later) has a lower value than that attained in regular silicate glasses [4].

Among the chains of the network-forming SiO_4-tetrahedra (which form a series of
covalent atomic bonds along a chain of ions: Si–O–Si) are the less abundant phosphorus
PO_4-tetrahedra [4]. Previously it was often assumed that the PO_4-tetrahedra would
be merged into the network formed by the silicon SiO_4-tetrahedra by forming similar
covalent bonds with the oxygens of adjacent tetrahedra as they do [4]. However, the
latest research suggests that the phosphorus is apparently *not* covalently bonded to
the Si–O–Si-chains (i.e. Si–O–P-bonds do not exist in the structure, at least in any
substantial amounts [4]) and instead the PO_4-tetrahedra are only loosely bonded to
other ions and are in essence separate from the actual network of covalently bonded ions
[4]. Depending on the relative quantities of ions in the composition of the material, the
PO_4-tetrahedra on some occasions seem to coalesce together to form somewhat larger
clusters of *ortophosphate* (PO_4^{3-}) within the network [4]. Predominantly though, the
PO_4-tetrahedra appear to be randomly scattered among the Si–O–Si-chains and are
on average separate from each other [4]. Similarly, the Na^+ and Ca^{2+} are randomly
distributed throughout the structure, forming ionic bonds (e.g. Si–O$^-$Na$^+$) at the ends
of the chains, often with several NBO's from separate Si–O–Si-chains simultaneously
(e.g. Si–O$^-$Ca^{2+}O$^-$–Si), thus altering the orientations of the chains [4].

The formation of an amorphous atomic structure can be summarized by starting
from the molten phase of, for example S53P4. In this high-temperature liquid, already
containing all the elemental constituents (e.g. Si and P) of the material, the movement
of atoms is very swift and the mutual arrangement of atoms alters rapidly, but nonethe-
less their overall – average – positioning resembles the amorphous structure formed at
lower temperatures [4]. As the material is quenched, i.e. cooled rapidly, a network of
silicon SiO_4-tetrahedra is formed, containing all the elemental silicon [4]. The network
modifiers Na^+ and Ca^{2+}, and to a certain degree the simultaneously formed phosphorus
PO_4-tetrahedra, however come to affect the formation process by redirecting a portion
of the Si–O–Si-chains towards the modifiers, due to the electrical charges of the ions
[4]. This process results in the formation of a SiO_4-network that contains substantial

cavities, enclosing the modifier ions Na^+ and Ca^{2+} within them [4]. In a similar way, the PO_4-tetrahedra – some of which are clustered together – are encircled by the long Si–O–Si-chains from all directions [4]. The end result of the formation process above is an amorphous structure in which the principal SiO_4-network is relatively sparse and the structure contains substantial amounts of (comparatively) loosely bonded ions [4].

The reason that the intricate details of the structure are of importance is the fact that the dissolution properties of the material – in the amorphous phase – are almost directly dependent on the distribution of the Na^+ and Ca^{2+} ions, and additionally of the PO_4-tetrahedra, since the water molecules H_2O involved in the dissolution process are more prone to instigate the dislodgement of these ions from the atomic structure, instead of the more rigidly bonded SiO_4-tetrahedra [4]. As the H_2O-molecules are able to diffuse deeper into a sparse network of relatively long Si–O–Si-chains, the dissolution of the ions is not constrained to the outermost surface layers of the material only, and instead the process will continuously advance deeper into the structure [4]. The result is a rapid surge of Na^+ and Ca^{2+} ions – as well as dissolved phosphorus – into the surrounding fluid, as compared to the dissolution rates of similar elements in glasses other than bioactive glass [4]. Eventually, the silicon contained in the SiO_4-tetrahedra will also be dissolved into the bodily fluids, but this process is considerably slower, and involves an intermediate stage of *silica gel* formation [4].

The network-modifier ions Na^+ and Ca^{2+} therefore affect the dissolution properties of the material by causing a modification in the overall atomic structure otherwise formed by the more abundant network-forming ions, and due to the relative sparseness of the network thusly formed, the network-modifier ions are then easily detached from the atomic structure during the dissolution process by the water molecules that are able to permeate deep into the cavities formed in between the chains of the network-forming ions [4]. The exact elemental composition of the bioactive glass is therefore of utmost importance, as even a slight alteration in the relative amounts of network-forming or network-modifier ions can have a significant impact on both the atomic structure and the dissolution properties of the material [4].

The composition of a bioactive glass, for example that of 45S5 or S53P4, is often expressed as percentages by weight (wt.%) of elements in the material, that is, as the relative overall weights of its elemental constituents, for example silicon or phosphorus (the weights of the oxygen ions are *incorporated* with each corresponding element in the fundamental *structural units*, for example SiO_2 or P_2O_5). However, a more descriptive expression would often be the percentages by *moles* (mol.%) of the elements (1 mole equals approximately $6.0 \cdot 10^{23}$ individual atoms) comprising the material, since many of the most important properties of the structure depend more on the actual number (i.e. a count) of separate ions (i.e. charges) in the overall atomic structure, rather than

Table 3.1: Elemental components of S53P4 and their relative amounts. Correspondence between percentages by weight (wt.%) [23] and percentages by moles (mol.%) [4]. (Oxygen is incorporated in the Structural units, which delineate for the ions of each element the atomic bonding with O-ions).

Element		Z	Structural unit	wt.%	mol.%
Silicon	Si	14	SiO_2	53.0	53.9
Sodium	Na	11	Na_2O	23.0	22.7
Calcium	Ca	20	CaO	20.0	21.8
Phosphorus	P	15	P_2O_5	4.0	1.7
(Oxygen)	O	8	(See above)	—	—

on the relative weights of the individual ions, although their relative *size* also increases (on average) with the ascending *atomic number* (Z). Therefore, a table of conversion from weight (wt.%) to molar quantities (mol.%) for bioactive glass S53P4 is included (Table 3.1).

A notable disparity between the two columns of the table is the difference between the percentages by weight (wt.%) and percentages by moles (mol.%) of phosphorus P. This is mainly due to the structural unit *phosphorus pentoxide* (P_2O_5), which contains more oxygen-ions relative to the amount of cations in the unit. The structural unit P_2O_5 is used in this context, although in the actual structure the PO_4-tetrahedra are often isolated and hence do not contain more than one P-ion. In a similar fashion, the structural unit *silica*, SiO_2, is used, although individual SiO_4-tetrahedra are most often linked to only two adjacent tetrahedra instead of four as in *vitreous* silica [4].

The connectivity NC_{Si} of the Si-network can be quantified with the formula [4]

$$NC_{Si} = \frac{4 \times SiO_2 + 6 \times P_2O_5 - 2 \times (M_2O + M'O)}{SiO_2}, \tag{3.1}$$

in which M_2O and $M'O$ are the network-modifier structural units [4]. By this definition of the network connectivity NC_{Si}, the atomic structure of for example plain, vitreous silica has a value $NC_{Si} = 4$, and the quantity NC_{Si} decreases as the network-modifier content increases, culminating in the bioactive glasses that typically have a NC_{Si} value between 2 and 3, for example 45S5 has a value $NC_{Si} = 2.11$ [4]. For S53P4 the network connectivity attains a value $NC_{Si} = 2.54$, which means that a Si-ion is connected – *on average* – to 2.54 other Si-ions, via the shared Bridging Oxygen-ions [4].

During the rapid cooling (i.e. quenching) of the molten precursor of a bioactive glass, an amorphous atomic structure is most preferentially adopted by the material. However, a *crystalline* atomic structure of the material also exists, and under certain conditions the amorphous atomic structure can (partially) *transform* into this phase, which can have a detrimental effect on the dissolution properties of the material, and as a consequence, also on its *biomedical* properties [4].

3.2.2 Crystallization Tendency of Bioactive Glass

The manufacturing process of a bioactive glass scaffold comprising a large amount of small granules often involves a *molten precursor* that contains precise amounts of the predetermined elemental components intended for the solid phase of the glass [24]. The molten precursor is then quenched, i.e. cooled rapidly, to produce a sizeable temporary object of solid, amorphous glass, which is then crushed or even pulverized down to the preferred size range of the granules [24]. The granules are then – in effect – aggregated together to form a compact pellet by exploiting the properties of glass-like substances.

Below the melting point T_l of a bioactive glass, above which the material is in a liquid form, there exists a temperature range in which the material is in a semi-solid state that is still relatively malleable, allowing for the material to be easily deformed (at the micrometre length scale) in order to e.g. *fuse* separate granules of the glass together by a combination of moderate heat and applied pressure in a process of sintering [4].

The temperature range in which this type of processing is possible, is however quite narrow for the bioactive glasses due to their amorphous atomic structure [4]. If the limit of the temperature range is exceeded, a process of spontaneous *crystallization* may occur, thus transforming the previously amorphous atomic structure into a crystalline structure that has the exact same elemental composition, but often a different overall density [4]. As the contrast in x-ray microtomography images is determined by both the elemental composition *and* the density of the material, the resulting brightness of a crystallized portion of bioactive glass in the reconstructed 3D-images would hence be different from the main amorphous portion, although in reality difficult to discern [6].

The main problem in *biomedical* terms, however, would be the lack of *bioactivity* in the crystallized portion of the bioactive glass, in e.g. individual granules that have for some reason transformed into the crystal phase [35]. This is due to the *dissolution* properties of bioactive glasses, which are markedly different in a crystal phase – in which significantly less occurs – and in an amorphous phase, in which the dissolution process progresses rapidly and is in effect the initial *cause* of all resulting bioactivity in the material [4].

3.3 Dissolution Properties of Bioactive Glass

The detailed description of the amorphous atomic structure of bioactive glasses, provided in Subsection 3.2.1, is in practice a pre-requisite for understanding the *dissolution* and *precipitation* behaviour of the material, initiated when a scaffold of bioactive glass is implanted into the site of an injury in the bone (e.g. a femur) and is hence subjected to bodily fluids surrounding – and in effect inundating – the implant and the defect as

a whole [4].

When an object consisting of bioactive glass is subjected to fluids that contain water molecules, the dissolution of its constituent elemental components commences immediately [4]. Water molecules are intrinsically capable of dislodging ions from the atomic structure, and as the amorphous atomic structure – most often adopted by bioactive glasses – is relatively sparse, i.e. *open*, the dissolution process can easily advance deep into the structure [4].

The modifier ions of the amorphous atomic structure (Subsection 3.2.1), i.e. the Na- and Ca-ions (and the PO_4-tetrahedra bonded to other ions by loose atomic bonds) are dislodged more easily than the network-forming Si-ions and are therefore dissolved immediately by large numbers [4]. As a result, the Ca-, Na- and PO_4-content in the surrounding fluid, to which the object of bioactive glass is inundated, rises formidably in a very short amount of time [4].

This process will commence regardless of the composition of the *fluid*, as long as it contains abundantly water molecules [4]. In bodily fluids, the Ca- and Na-content is already significant even at regular levels (i.e. when the tissue is *not* inflammated) [4]. However, the added concentration will aid the healing process which starts immediately after an injury, and the ions Na and Ca can then be labeled as *therapeutical ions*, beneficial to the healing process in general [4].

The Na- and Ca- (and P)-ions will also raise the *osmotic pressure* of the fluid, which – in addition to a raise in the pH-level of the fluid – has beneficial effects on the *antibacterial* properties of the material [23], properties especially prominent in S53P4.

A portion of these ions will eventually *precipitate* back onto the surface of the material and instigate the formation of a *silica gel* layer on the outermost surface of the material, while the dissolution process all the time continues within the atomic structure, with water molecules diffusing and permeating ever more deeply into the structure [4].

3.4   Formation of Silica Gel Layer

It should be emphasized that the dissolution of the bioactive glass, the precipitation of certain chemicals back onto it, and the formation of various reaction layers, all alter the density and the elemental composition of the material at these locations, therefore also altering their contrast in the x-ray microtomography images.

Following the initial major release of Na-, Ca- and P-ions from the outermost layers of the amorphous atomic structure, a *second stage* in the dissolution and precipitation process, i.e. the chemical exchange between the fluid and the scaffold, ensues [4]. This next stage involves the precipitation of some of the chemicals *back* into the

amorphous atomic structure, with some additional chemicals from external sources, for example bodily fluids, included [18].

As the Na^+- and Ca^{2+}-content of the fluid increases, the pH-level changes accordingly, and a simultaneous *cation exchange* on the surface layers of the amorphous atomic structure ensues, with H^+-ions – originating from the water molecules H_2O – replacing a portion of the original modifier ions at the ends of the chains of Si-tetrahedra [18]. The process can be expressed as: $Si-O^-Na^+ + H^+ + OH^- \rightarrow Si-OH^+ + Na^+(aq) + OH^-$.

As a result, a cation-depleted region will form near the surfaces of the amorphous atomic structure that are in direct contact with the surrounding fluid [18]. The hydroxide ions OH^-, abundant in the pH-elevated fluid, will then begin to break the covalent Si–O–Si-bonds in the overall network structure, resulting in the formation of yet more Si–OH-bonds on the surface layers [18].

This will lead to a *repolymerization* in parts of the silica network, which means that the structure of the silica is transformed into a *silica gel* (containing *silanol* groups Si–OH) [4]. The silica gel has a markedly different elemental composition and density as compared to the previous amorphous structure of the undissolved bioactive glass, in that it contains only silicon Si, oxygen O and hydrogen H, the latter originating from the water itself [4].

The formation of the silica gel layer on the surface of the bioactive glass will then enable the precipitation of some of the calcium Ca- and phosphorus P-ions back onto the newly formed layer, subsequently forming a layer of hydroxycarbon apatite (HCA) on top of the silica gel layer, which in turn enables an efficient *bonding* with newly formed bone [4]. The dissolution of the bioactive glass will, however, continue in the amorphous atomic structure due to the sparseness of the network, which in effect prevents a completely *isolating* surface layer to be formed on the granules [4].

The process described so far will progress in a similar fashion regardless of the surrounding tissue or exact composition of the fluid, and will in fact be similar in an *in vitro* environment, that is, in a test tube or an equivalent dish used in laboratories [18]. Even the formation of the HCA-layer is feasible in such an isolated fluid, as long as it contains enough proper chemicals [18]. The formation of the *bone* on top of the *reactive layers* of silica gel and HCA will however require the presence of living cells, a process which will be described in the next Section 3.5.

3.5   Reaction Layers on BAG-S53P4 Granules

As has already been discussed in Sections 3.3 and 3.4, the rapid dissolution of Na-, Ca- and P-ions from the amorphous atomic structure of the bioactive glass BAG-S53P4 leads to the formation of a silica gel layer on the outermost surface of the granules [4].

Initially the silica gel layer is only a few atomic layers thick, but since the dissolution and hence also the silica gel formation proceeds incessantly into the amorphous atomic structure, the thickness of the layer is soon discernible in the µCT-images [4]. As the length scale of the granules is in the millimetre range, a typical thickness of the silica layer in the Middle Stages of development (See Figure 1.3) is tens of micrometres.

Simultaneously, as the dissolution and the silica gel layer formation continues, a portion of the dissolved Ca^{2+}-ions and PO_4^{3-}-groups begin to precipitate *back* onto the silica gel layer, conceivably *nucleating* on the Si–OH-groups on the surface of the silica gel [18]. Through intermediate stages of octacalcium phosphate crystallites and an amorphous calcium phosphate formation, a crystalline structure of hydroxycarbonate apatite (HCA) is eventually formed [18]. The chemical formula of plain hydroxyapatite (HA) can be expressed as $Ca_5(PO_4)_3(OH)$, in which either PO_4^{3-} or OH^- is *substituted* by carbon group CO_3^{2-} in HCA [4]. Similarly as the silica gel layer, the HCA layer continues to grow in thickness during the progress of the dissolution process [4].

These two *reaction layers*, the silica gel layer and the HCA layer, therefore *envelop* the slowly dissolving – and shrinking – bioactive glass granule in an *encasement*, which however allows water molecules to permeate through [18]. Due to inherent disparities between the *rates* of the processes, the end result could be a thin HCA layer surrounding a granule consisting solely of silica gel, or even a completely hollow *shell* of HCA, still separate from the nearby formations of newly grown bone [18]. In most cases though, a layer of bone begins to form *onto* the HCA layer, facilitated by the similarity of the structure of HCA and the *bone mineral* (See Introduction 1.2), since the cells involved in the formation of bone interpret the HCA layer as pre-existing bone [18]. This layer of newly formed bone then advances into the retreating silica gel layer – which is also gradually dissolved – and eventually occupies the entire volume of the former granule of bioactive glass [18]. As the granules of the porous scaffold have initially been in an arrangement that in fact resembles a *trabecular structure*, and the bioactive glass is effectively *replaced* by the newly grown bone, the final structure can reasonably be referred to as trabecular bone – although in the end it will be remodeled into a cortical structure resembling the original bone.

After the three-dimensional network-structure of newly formed trabecular bone has been formed, to initially encompass and then progressively replace the bioactive glass granules, the overall healing process of bone continues in the manner described in the Introduction 1.1 and 1.5 (Figure 1.3). The structures of bone and the thicknesses of the reaction layers formed during the Early, Middle and also the Latter stages of development are all innately at the micrometre length scales, and are therefore located at the prime range of resolution for the x-ray microtomography measurements.

Part III

Measurements

4. Measurements

The series of x-ray microtomography measurements for the set of rabbit femur bone samples was conducted in University of Helsinki's Laboratory of Microtomography at the end of 2018 and the beginning of 2019. The measurements for all of the 34+3 samples were performed with the laboratory's Nanotom-apparatus, designed to be easily and reliably handled by even an unexperienced user.

At the time of the measurements, the apparatus consisted of a General Electric Phoenix Nanotom x-ray tube, an x-ray detector and a movable rotating platform for the sample to be measured on, all positioned in an enclosed and protected measurement cabinet. An integrated system control (`xs|control`), image acquisition (`datos|x`) and reconstruction (`datos|x`) software, which was used in conjunction with the apparatus, was provided by the manufacturer.

The measurements were performed with exactly the same parameters for each sample, as it was considered to be of utmost importance that the resulting images would be as comparable with each other as possible. A few test measurements and trial reconstructions were performed in order to establish a proper voltage, current and positioning (i.e. magnification) for the samples. The parameters for the measurements are summarized on Table 4.1.

The values of the parameters were chosen to enable the bone to attain an optimal contrast with the bioactive glass granules, and thus disregard the softer tissues, that

Table 4.1: Parameters for the measurements. All samples were measured with the same parameters. The Distances FDD and FOD refer to the Focus–Detector (i.e. Source–Detector) and Focus–Object (i.e. Source–Sample) distances respectively. Binning of the detector pixels was 2×2 for all samples.

Parameter		Value	Unit	Parameter		Value	Unit
X-ray Tube Voltage	V_p	80.0	kV	Distance FDD		30.0	cm
X-ray Tube Current	I	150.0	µA	Distance FOD		4.5	cm
Integration Time	T	250.0	ms	Magnification	M	6.7	—
Frame Averaging		10	—	Voxel Size (Cubic)	V	15.0	µm^3
Number of Projections		1000	—	Al-filter Thickness		1.0	mm

Table 4.2: Parameters for the reconstructions. Most samples were reconstructed with varying parameters. The values of some parameters varied due to the independent movement of individual samples. The reconstruction software was `datos|x-reconstruction`, included in the Nanotom-apparatus.

Parameter/Module	Value	Status
Beam Hardening Correction	0	Disabled
Ring Artefact Reduction	—	Enabled
Automatic Geometry Calibration	Varies	Enabled
scan|optimiser	Varies	Enabled

some of the samples apparently still contained, entirely. On the other end of the density – and elemental composition – scales was the metal plate and the metal wire that some of the samples contained. By selecting the parameters to enhance the contrast between the bone and granules, the x-ray beam had to be adjusted to a voltage that did not quite have enough energy to penetrate the metal parts efficiently. This resulted in the *beam hardening* phenomenon to take effect, but considering the alternative, in which the contrast between the bone and granules would have been minimal, the resulting *artefacts* were estimated to be a lesser problem in the subsequent analysis of the measurements. An aluminium *filter* with thickness 1.0 mm was placed on the path of the x-ray beam to decrease the impact of the beam hardening phenomenon, but this alone could not eradicate the effect completely. (See Chapter 2 for reference.)

It was then decided that an effort to reduce the artefacts was to be made, and therefore, at this point, the focal theme of this entire Thesis was established, and the reduction of the artefacts became the main issue to be solved, for it was also clearly evident that the subsequent segmentation of the resulting images might not be feasible unless the artefacts were successfully reduced, or even completely removed, first. This was to be accomplished by a combination of *post-processing* methods and techniques, applied to the already reconstructed images of the samples. As the reconstruction method, the software provided by the manufacturer of the apparatus was used (4.2.2).

4.1   Samples

The samples were delivered to the Laboratory of Microtomography in closed plastic test tubes with only the sample identifiers as labels and without any additional information regarding the contents of the samples. They were then kept for safeguarding in a plain sample-refrigerator for a period of few months.

All of the plastic test tubes had been flooded with a liquid to preserve the biological components of the samples, i.e. remnants of softer tissues, which some of the samples

still contained. Care was taken not to open the test tubes unless it was unavoidable in order to readjust the samples to a stable position during the measurements.

The samples could immediately be divided into two distinct categories by visual inspection alone, since a portion of the samples contained only a separate individual implant, while the main portion of the samples seemed to contain an implant that had been enveloped – to varying degrees – by newly grown bone protruding from the ends of a segmented femur bone. On all of these bone-containing samples, attached to the bone was also the original *metal plate* that had been supporting the femur during the healing process. An additional *metal wire* was also included in some of the samples.

4.1.1   Samples Containing Metal Plates and Wires

Altogether 24 samples of the total 37 samples contained a metal plate, and 17 of these additionally contained a metal wire around the scaffold of BAG-S53P4(-PLGA), or on some samples a cylindral block of PMMA, that were implanted between two separate sections of a femur. On Figure 4.1 are radiographs from a typical sample containing the metal plate and the wire.
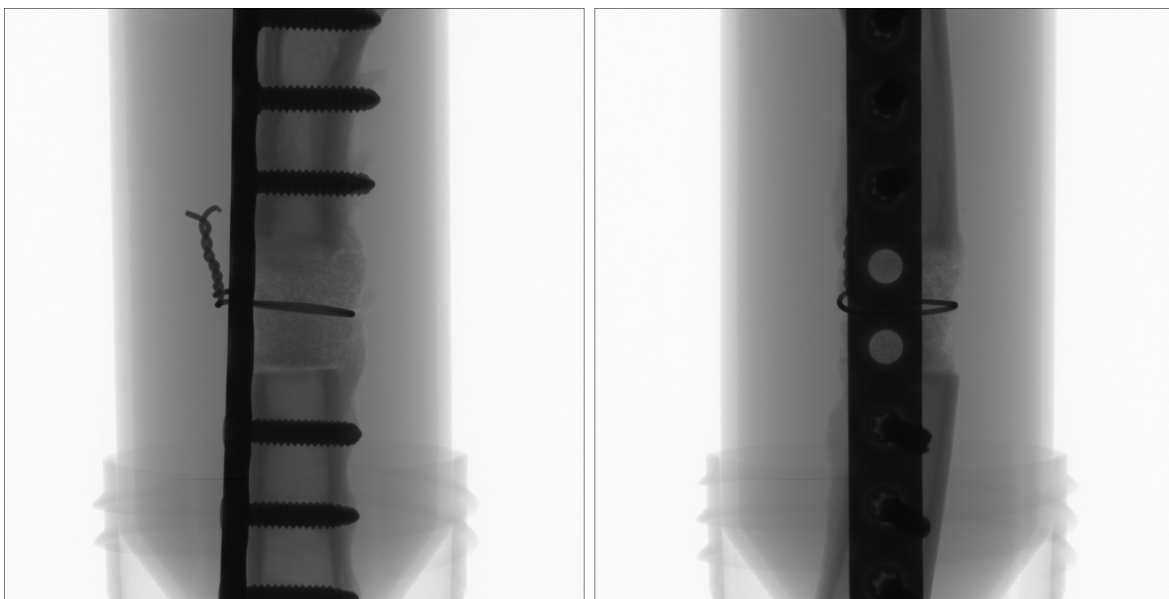
Figure 4.1: Two *conventional* x-ray scans of sample D13 from two different viewing angles, conducted prior to the actual x-ray microtomography measurements. The source-to-sample distance was 130 mm on both scans. Visible on both radiographs is the plastic test tube – containing the sample and the liquid surrounding it – placed on top of another similar test tube to conveniently raise the level of the sample into the x-ray beam. **At left**, the side profile of the *metal plate* and the *metal screws* attached to the femur are visible, as is the *metal wire* holding the scaffold firmly in position. **At right**, the two empty *screw holes*, which are similarly adjacent to the scaffold on every sample containing the metal plate, are clearly visible. The width of the plastic test tube is approximately 28 mm. The volume from which the actual x-ray microtomography 3D-images were acquired is delineated on Figure 4.2.
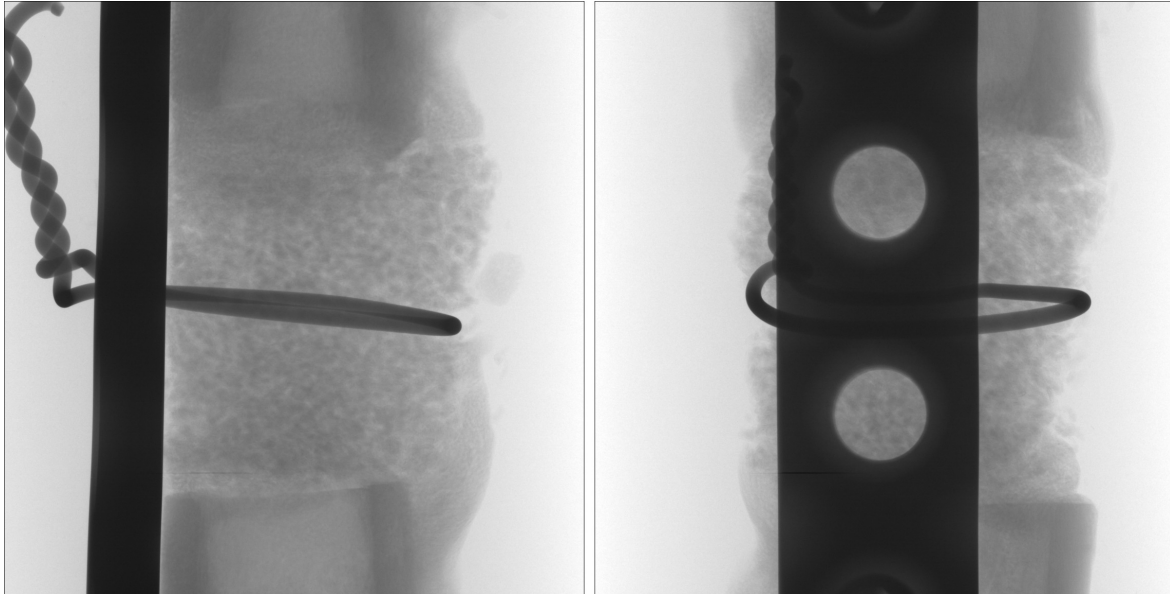
Figure 4.2: Radiographs of sample D13 with a source-to-sample distance of 45 mm, delineating the volume of the sample from which the actual x-ray microtomography 3D-images were then acquired. A similar structure consisting of metal parts can be found on a large portion of the samples, causing severe *metal artefacts* on the reconstructed 3D-images. By convention, the gray-scales in the radiographs are *inverse* as compared to the gray-scales on the reconstructed x-ray microtomography images, and therefore, for example, the *dark* metal on the radiographs is intensively *bright* in the µCT-images.

The metal plate was manufactured from standard medical-grade steel (mainly composed of iron Fe and small amounts of carbon C) which in itself is – in a biological sense – effectively inert. An array of sizable screw holes had been drilled throughout the length of the plate to accommodate – in these samples – six screws (with a similar composition as the plate) which attached the femur to the plate. On each sample two screw holes, adjacent to the scaffold in between the segments of femur, were left empty. To minimize the movement of the scaffold in the early stages of the healing process, an additional metal wire (with possibly a dissimilar composition as compared to the metal plate and the screws) had been wrapped around the scaffold on some of the samples.

The details of the metal structures are of great importance, as they cause severe *metal artefacts* on the x-ray microtomography images, and the degree to which these artefacts degrade the quality of the image – in a particular location – depends directly on the proximity of the metal objects to the region of the image containing any objects of interest. On Figure 4.2 the volume from which the x-ray microtomography images were acquired is delineated, and the proximity of the metal plate to the entire other half of the scaffold, at left, and the metal wire to the central edge region of the scaffold, can be clearly observed.
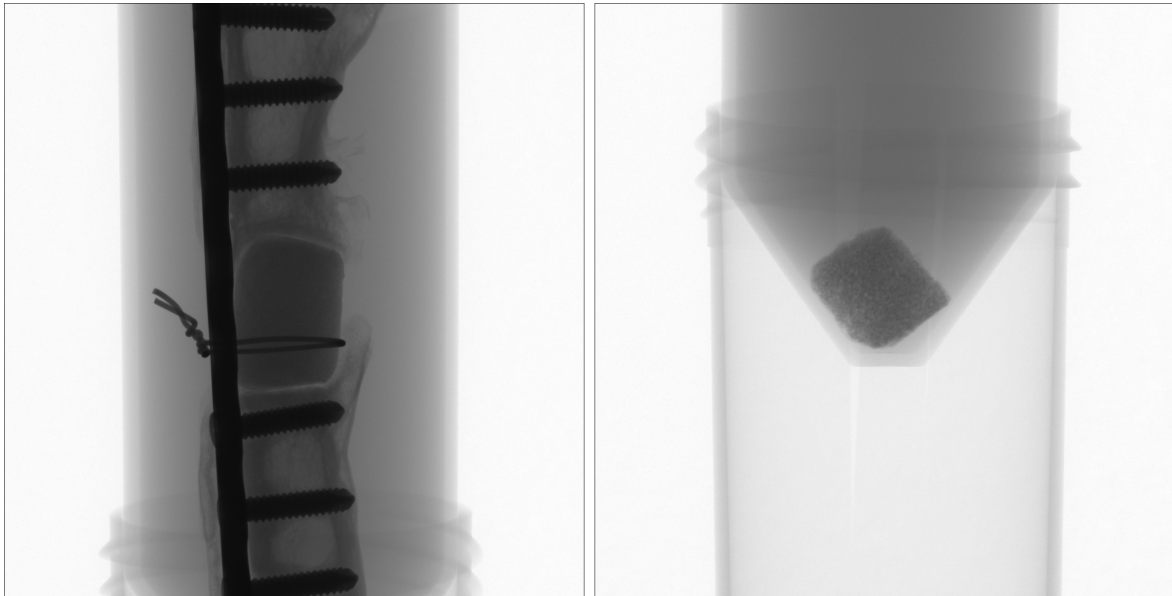
Figure 4.3: At left, a radiograph of sample D35 containing a PMMA-implant instead of a bioactive glass implant composed of BAG-S53P4(-PLGA). **At right**, a radiograph of sample D18, a scaffold comprising BAG-S53P4, which has been *detached* from the metal support it was initially attached to.

4.1.2 Samples Containing Plain Scaffolds

As was already previously mentioned, 10 of the 37 samples contained only a separate scaffold that had been detached from a similar metal plate, and possibly metal wire, construction as on the other 24 samples. This may have been due to the incessant and in practice unavoidable movement of the rabbits during the early stages of the healing process, preventing the initial bonding of the scaffold and the bone to proceed properly. Nevertheless, these samples still contained valuable information on the precise *reason* why they had not remained in their intended position, while the other similar scaffolds in fact had. Therefore, the x-ray microtomography measurements were conducted with the exact same parameters (Table 4.1) for the plain samples (Figure 4.3, at right) that were used for the other 24 samples containing the segments of femur and the metal plate and wire.

4.1.3 Samples for Comparison

To provide a comparison for the scaffolds which had been subjected to a biological environment, that is, implanted into a defect-containing femur of a rabbit, three unused scaffolds were delivered among the other 34 samples, described in the previous Subsections 4.1.1 and 4.1.2. No *calibration phantom* [7] for the bone was available.

These unused scaffolds were similar to the scaffolds which had been implanted, in that one scaffold contained only the granules of bioactive glass BAG-S53P4, while

the other two BAG-S53P4-PLGA scaffolds were incorporated with a surface layer of the biodegradable polymer PLGA that had a thickness of 200µm on one scaffold and 600µm on the other, hence forming a thin PLGA polymer *coating* on the samples.

It was later revealed – after the measurements had already been performed – that in general the other 34 samples contained the same three distinct types of scaffolds: BAG-S53P4$_{uncoated}$, BAG-S53P4-PLGA$_{200µm}$ and BAG-S53P4-PLGA$_{600µm}$. Additionally, the *control* samples that contained an inert PMMA-implant were included in the 34 samples, which were *harvested* (that is, removed from the rabbits) at three different stages, i.e. *time points*, that were either 2, 4, or 8 weeks after the initial implantation of the scaffolds. At each time point, three samples of each type were harvested. Unfortunately, some of the rabbits deceased prematurely, and therefore the total amount of samples is 34 instead of 36.

In a sense, the samples containing the control implant composed of PMMA could also be regarded as samples for comparison. These 7 control samples (two of the rabbits had deceased prematurely) had been harvested from the rabbits at the same stages of development, i.e. time points, as the rest of the samples, that is, at 2, 4 or 8 weeks of healing and bone regeneration. The biologically inert PMMA-implant will in due time be *enveloped* by a structure of newly grown bone (Figure 4.3, at left), which however remains thin and fragile and resembles more the initial *callus* developing around a fresh defect site [19], a structure of bone that is normally *resorbed* in the latter stages of the healing process. The simultaneously forming membrane around the PMMA-implant is utilized in the *two-stage induced membrane*-technique [36].

4.1.4   Preparation of the Samples

All the 34 samples were designated to be sent for further analysis after the µCT-measurements had been performed, conducted with various different techniques and measurement methods, for example with ultrasound propagation imaging, and were ultimately destined for scanning electron microscopy and a histological analysis in which the samples are first dissected apart and then analysed.

Therefore, as little preparation as possible was performed on the samples prior to the µCT-measurements. However, some of the test tubes had to be opened as some of the samples contained, for example, an exceptionally *thin* femur that needed additional support, since the slowly rotating platform caused the sample to *sway* slightly during the measurements, which could have a detrimental effect on the quality of the images.

For this purpose, a plastic supportive structure was constructed from a thin, hollow and elastic plastic tube which was attached with water-resistant glue to a severed end portion of a similar test tube that contained the samples. Due to the elasticity of

the supportive structure, the cap of the test tube then gently pressed the sample via the plastic tube, exerting a minimal pressure on the samples containing fragile bone, yet firmly holding the sample in place during the measurements.

4.2   Measurement Equipment

The equipment that was used in the x-ray microtomography measurements, that is, the *hardware* consisting of x-ray tubes and detectors and other technical tools, is described in this Section, along with the reconstruction *software* that was utilized in creating the final μCT-images.

Both the hardware used in the μCT-measurements and the software used for the reconstructions were essentially unmodified and represent in every way standard tools in the field of tomography. They therefore constitute a typical example of the equipment that is in regular use at most tomography laboratories.

4.2.1   The Nanotom Apparatus

The Nanotom apparatus at University of Helsinki's Laboratory of Microtomography consists of a GE Phoenix|X-ray Systems Nanotom NF 180 x-ray tube, a Hamamatsu detector and a specifically tailored movable platform including a rotating sample-holder, all placed inside a large lead-protected measurement cabinet. An integrated software for system control (`xs|control`), provided by the manufacturer, controls the x-ray tube and the *manipulator* (CRC), while an integrated software for image acquisition (`datos|x-acquisition`), records the data from the detector. This arrangement enables a reliable and *repeatable* operation of the system, as the distances from e.g. the x-ray source to the sample or from the sample to the detector can be controlled with ease, thus providing reliability and increasing the *comparability* between the samples.

4.2.2   Reconstruction Software

The integrated reconstruction software (`datos|x-reconstruction`) of the Nanotom apparatus, provided by the manufacturer, was used to perform all reconstructions in this Thesis. (See Table 4.2 for the parameters used in the reconstructions.)

Unfortunately, the manufacturer does not provide a detailed account on the properties of the reconstruction software, only stating that it uses an optimised Feldkamp-algorithm, which should equate to a modified Filtered Back-Projection algorithm (Subsection 2.3.3). Also, the essential working principle of the additional Beam Hardening Correction algorithm was left undetermined, and for this reason, it was adjusted to a value of zero in the actual reconstructions, i.e. it was not used at all.

The Beam Hardening Correction algorithm (add-on *module*) of the software was tested on the samples on a few trial reconstructions, but its functionality on the samples that contained metal was not sufficient, since the algorithm introduced additional sharp *streaks* onto the reconstructed images that were quite pronounced and radiated from the metal to all directions, in essence covering the entire image. In addition, the algorithm was apparently not designed to reduce any of the excess brightness emanating from the metal, which cause the most severe problems for the quality of the images.

However, the Beam Hardening Correction module did function properly for the samples that did *not* contain any metal, reducing the excess brightness *within* the edges of the sample. Nevertheless, as the objective was to use the exact same parameters for every sample to increase their comparability, the usage of the module was in the end discarded with the actual reconstructions.

Part IV

Image Processing and Analysis

5. Image Processing

The processing of images constitutes a substantial portion of this Thesis, and numerous different image processing methods and techniques will be introduced in the following Chapter. For most of these methods, only a brief description of their general properties will be presented in the following pages, and a more comprehensive characterization of certain essential methods and their properties will be provided on Appendix A. As an example, a Figure illustrating the relationship between a *stack* of images and the *slices* it contains – in various orientations – is provided in the Image Processing Supplement.

The image processing methods utilized in this Thesis are for the most part already well-established and routinely employed in the field of image processing. For example the method of *thresholding* an image – relying on its *histogram* – and creating a *binary mask* of the thresholded image, for which further processing can be applied to, is an indispensable technique for segmenting an image into its constituent elements or objects of interest. Another commonplace technique is the *filtering* of an image to reduce the noise inherent to the initial x-ray measurements. Filtering is also used to achieve an enhanced contrast between the objects in the image, thus enabling for example the thresholding to accomplish a more accurate result. Various different image processing methods and techniques can – in a similar fashion – be combined into an arbitrarily long sequence of consecutive steps or stages, i.e. a *workflow*, that can then be applied to all the images in turn, performing the exact same procedure or sequence of actions on every sample.

Two such workflows or combined methods will be introduced in the next Sections, constituting the quintessential contents of this Thesis. First of these methods concerns the reduction of image artefacts, mainly due to the presence of metal, and one separate and somewhat more extensive method covers the subsequent segmentation of the image into areas or volumes, i.e. *regions*, that contain either bone in distinct growth patterns or granules at different stages of development (see Chapters 2 and 3 for reference). In fact the second method is composed of three distinct stages, each segmenting out a different portion of the image, but as these are closely interlinked and their functionality depends on the previous stage, they can all be considered as one combined method for the segmentation of the image.

The first and primary method (Subsection 5.2.3: Method for Reducing Metal Plate Artefacts) introduced in this Thesis utilizes a novel combination of sequential Gaussian filterings, applied to segmented regions of the image determined by binary masks from consecutive thresholdings, which are then systematically subtracted from each other and in the end added together to form a correction image, to be subtracted in turn from the original image that still contains the actual artefacts.

Although a second separate method was planned as an additional correction for images that contain streaks of excessive brightness due to the presence of metal wires, the development of the method did not proceed at the same pace as the development of the first, and therefore its implementation was postponed for the future. The method would have utilized an algorithm, referred to as the Convex Hull, that isolates the outer limiting edges of a mathematical structure enclosing the area between separate portions of the metal. These lines connecting the corners of the metal – in the transverse plane – would have then *focused* a Gaussian filtering of the metal that would have produced a new correction image to be added to the first one.

A third planned method would have utilized the *background* outside the area of the actual sample to calculate an adaptive correction term for the artefacts encircling the outer edge of a sample, typically pronounced in most dense samples. The application of this method would be most often required in the samples that do not contain any metal parts in them.

5.1   Reconstructed Images

The images to be processed in the above described manner are the three-dimensional reconstructions created from the circa 1000 (per sample) two-dimensional conventional x-ray scans conducted during the measurements, a procedure detailed in Chapter 2. These three-dimensional images, which are in essence *maps* (in 3D) of the attenuation coefficient of x-ray radiation inside the sample, can also be regarded as large *stacks* of two-dimensional *slices*, each slice portraying a cross-sectional area in, for example, the transverse direction of the sample. The fundamentally three-dimensional nature of the actual reconstruction can then be reduced to a semi-2D form, enabling the processing to be focused on one slice at a time. However, on certain steps in some of the procedures, a simultaneous 3D-processing of the entire stack is achievable. (See Appendix A.)

For processing the images, the freely distributed software *ImageJ* (version 1.52p) and its auxiliary *Fiji*-package was used [30][39]. In the following Sections, the image processing tools of *ImageJ* will be referred to in a `typescript` notation. Most methods introduced here are, however, in a sense universal in their nature and do not depend on the software used.
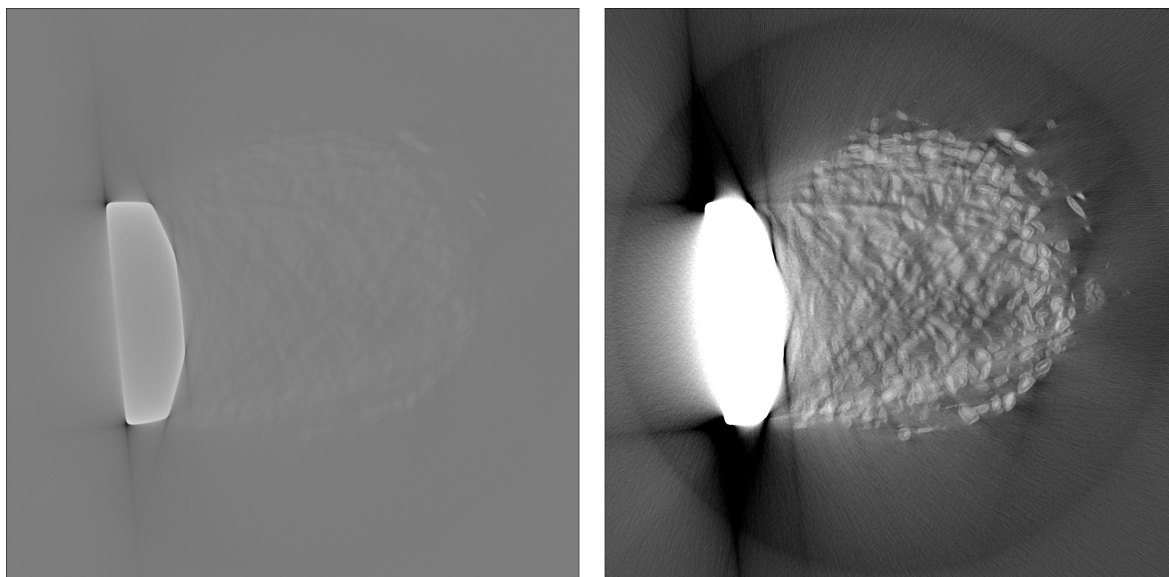
Figure 5.1: A transverse slice from sample D13 near the middle of the scaffold. **At left**, the initial scale of *Gray Values* emphasizes the metal plate near the left border. **At right**, the *same* slice, for which the `Brightness&Contrast` has been adjusted to better reveal the objects of interest, i.e. the bioactive glass granules. Metal artefacts, both bright and dark, near the metal plate are clearly visible.

5.1.1   Image Pre-Processing by Filtering

All images, that is, the entire 3D-images (each consisting of a stack of slices with a size of $1128 \times 1128 \times 1152$ voxels), were pre-processed with a three-dimensional median filter included in *ImageJ*, the `Median3D`-filter, with a radius of 2.0 voxels [30]. The tool used a $5 \times 5 \times 5$ kernel in 3D to calculate the *median value* in the immediate surroundings of *every* voxel and then changed the value of this voxel to the median value [30].

This procedure smooths the inherent *noise* in the images, but does not alter the values of brightness (*Gray Values*) of the voxels in the image excessively.
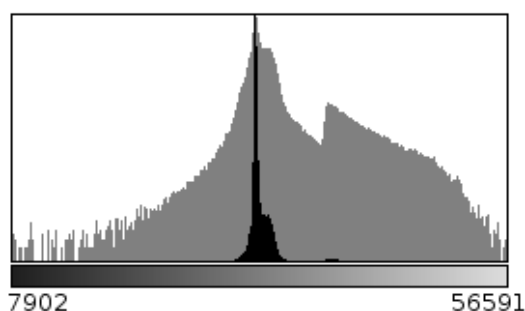
Figure 5.2: A histogram of the slice in Figure 5.1 which depicts the range and amount of gray values in the image. The large **black** peak corresponds to the amount of *background* pixels in the image. The **light gray** curve is a logarithmic scale superimposed atop the normal scale. The metal artefact on the lower edge of the scaffold adds brightness to the granules, causing the minor peak on the right.
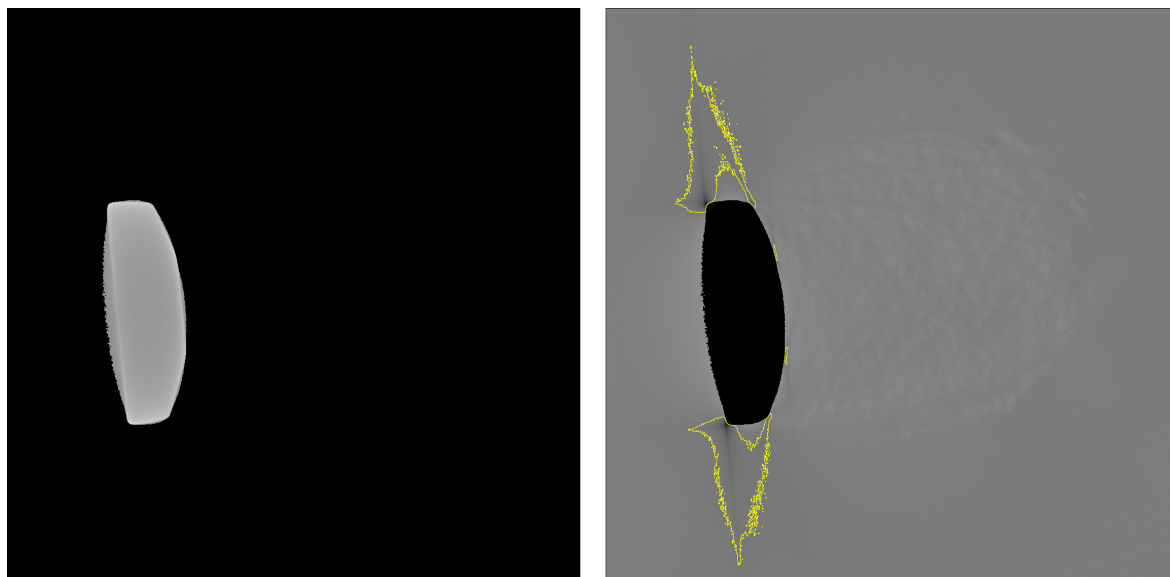
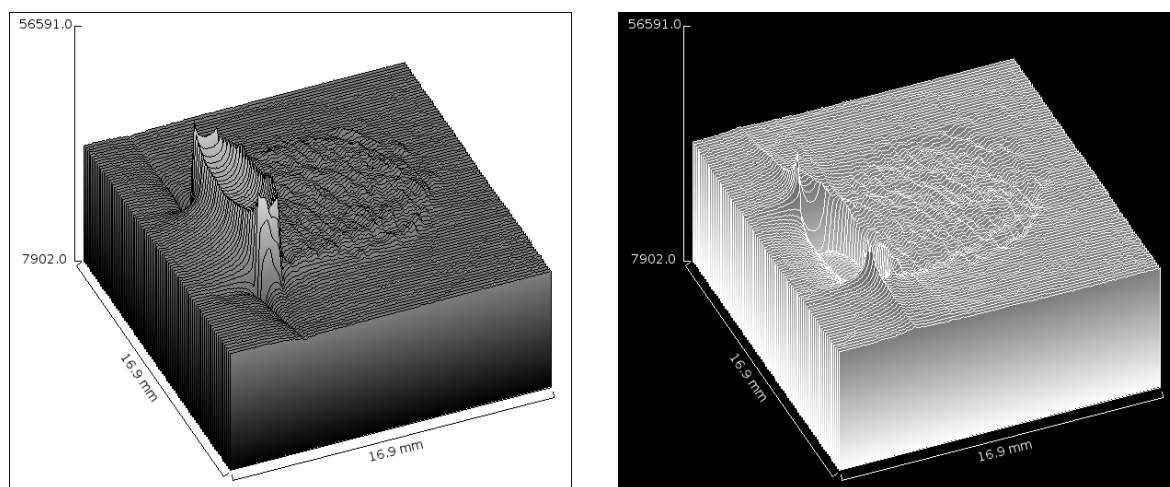**Figure 5.3:** **At left**, the slice from Figure 5.1 that has been *thresholded* by the algorithm Otsu, then the area outside the binary mask has been *cleared*. **At right**, the same slice in which the area *inside* the binary mask has been cleared. The yellow *overlay* depicts the borders of a subsequent thresholding by the algorithm Triangle, which isolates the area of the dark (*hypodense*) artefacts near the metal.

5.1.2   Image Thresholding and Binary Masks

Image thresholding was utilized extensively in the processing of the images, using the `Auto Threshold`-algorithms included in *ImageJ*. The process of thresholding utilizes the *histogram* of the image, which contains a distribution of all the *Gray Values* that an individual image contains. The x-coordinate of a histogram depicts the *Gray Values* and the y-coordinate portrays the *amount* of pixels (voxels) that the image contains for each value. (See Figure 5.2.)

Figure 5.4: 3D-surfaces of the slice from Figure 5.1, in which the *height* portrays the *brightness*. **At left**, normal scale. **At right**, *inverted* scale, revealing the structure of the dark artefacts.

Often the dark *background* of an image forms a substantial peak in the resulting curve, and the long tail to the higher *Gray Values* contains the actual objects of interest. (See Figure 5.2.)

A thresholding algorithm then calculates a value from the curve and transforms the image into a *binary mask* that contains only two values, the new minimum 0 and maximum 1, i.e. black and white. The voxels with brightness above the *threshold value* are turned white, and all other voxels are turned black. (See Figure 5.3.)

Numerous different thresholding algorithms have been developed for various purposes, each attempting to calculate a sought after location on the curve of the histogram in order to accomplish a *segmentation* of the image into regions of interest, for example granules and bone [40]. Some of the algorithms may have been originally developed for altogether different purposes, but nevertheless could be utilized on these images [40].

5.1.3   Binary Operators and Calculus

The obtained binary masks can be utilized in *clearing* regions from the images, after which the remaining image can be processed further, e.g. thresholded again.

The binary masks themselves can also be processed by e.g. *Dilating* or *Eroding* them on a pixel-by-pixel (or voxel-by-voxel) basis. Furthermore, the binary *operators* AND, OR and XOR can be utilized to combine, merge or separate the masks. Also, by *inverting* a mask, the functionality of the binary operator NOT can be achieved.
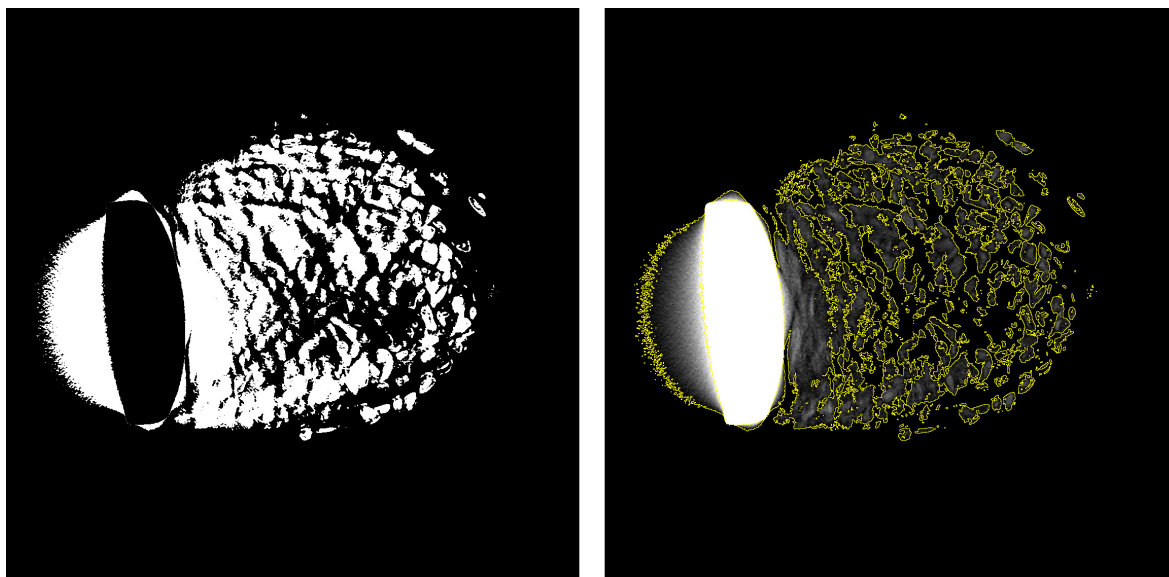
Figure 5.5: At left, a *manually* adjusted thresholding, resulting in a binary mask that incorporates the granules and excludes the metal, illustrating the nature of the problem with metal artefacts. **At right**, the same slice as at left (and as in Figure 5.1), but with adjusted contrast and an overlay of the binary mask at left. As can be seen on both images, threshold levels are difficult to adjust without interference from the bright artefact. Therefore, a *reduction* of the metal artefact is required.
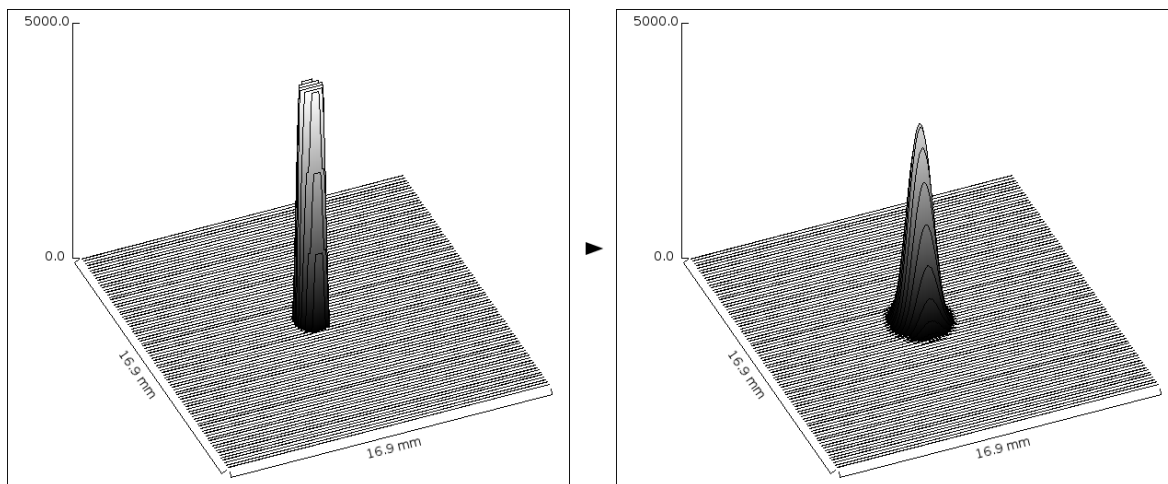
Figure 5.6: At left, a 3D-surface portraying an arbitrary circle with a *Gray Value* 5000. **At right**, the circle after a Gaussian filtering with a substantial radius $\sigma = 25$.

5.1.4   Gaussian Filter

The Gaussian filter has a substantial role in many image processing methods introduced in the next Section 5.2. Therefore, the equation defining a two-dimensional Gaussian function (Figure 5.6) in a general form is presented:

$$f(x,y) = A \exp\left(-\left(\frac{(x - x_0)^2}{2\sigma_X^2} + \frac{(y - y_0)^2}{2\sigma_Y^2} \right) \right), \tag{5.1}$$

in which A is a constant, and σ_X and σ_Y are the *variances* of the Gaussian function.

5.2   Reduction of Image Artefacts

The image processing workflows, that constitute the actual combined methods of this Thesis, mostly utilize the elementary methods introduced in the previous Subsections only. In fact, the first two methods for the reduction of image artefacts have already been presented in Subsection 5.1.2 as examples of thresholding.

5.2.1   Method for Thresholding the Metal

For the segmentation of the metal parts in all the samples that contained any metal, thresholding algorithm Otsu was utilized. The segmentation was not always precise, and bright regions that clearly were *not* metal were sometimes included, but with a similar clarity, *all* the metal *was* included to the segmentation on all the samples. Figure 5.3 shows a typical example on the precision of the algorithm.

5.2.2   Method for Removing the Dark Artefacts

For the separation of the dark *hypodense* [9] artefacts protruding from the corners of the metal (Figure 5.3), a combination of threshold algorithms Otsu and Triangle was utilized. First, the `Auto Threshold` algorithm Otsu [30] was used to create a binary mask that was then in essence *inverted* and utilized to *clear* the area *inside* the metal. Next, the `Auto Threshold` algorithm Triangle [30] was used to create a binary mask that delineates the dark artefacts from the image created by the inverted binary mask of Otsu.

An important feature in this procedure was that it established an anchored level of *Gray Value*, set immediately below the level of the background. This proved to be a useful quantity in the next steps of the artefact reduction process, since it created a self-adjusting *baseline*-level for each sample, that appears to be comparable between all the samples. Then, by *subtracting* this level from the overall *Gray Value* scale of the entire image, the remaining objects in the image can be directly utilized in the Gaussian filtering that follows.

5.2.3   Method for Reducing the Metal Plate Artefacts

The method for reducing the artefacts caused by the metal plate present in the majority of the samples is the principal method for metal artefact reduction in this Thesis. It has been developed in a stepwise fashion, following the internal logic of the procedure once it had become apparent. The procedure should not be considered to be complete or fully comprehensive, as new refinements may be discovered in the course of time.
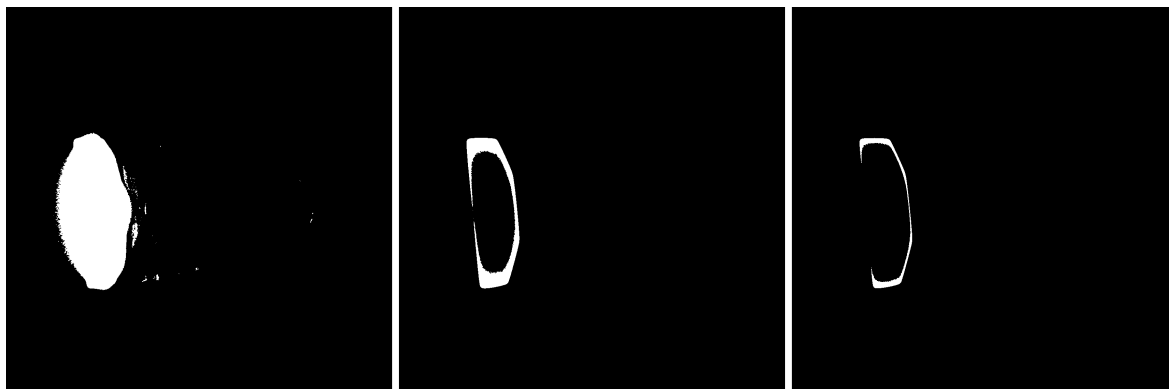
Figure 5.7: At left, the binary mask of the slice from Figure 5.1 produced by the threshold algorithm Yen. **At center**, the binary mask of the same slice produced by the threshold algorithm Shanbhag from an image *cleared* by threshold algorithm Otsu. **At right**, the binary mask produced again by Shanbhag from the previous one. The binary mask produced by Otsu has been presented on numerous previous Figures. The threshold levels are approximately 2000 . . . 4000 *Gray Value* apart, and these particular levels represent the first, the third and the fourth levels.

The working principle of the method can be outlined as follows:

- The baseline-level and the dark artefacts are determined as in Subsection 5.2.2.

- The first *pair* of `Auto Threshold` levels (*Gray Values*) and their concomitant binary masks are calculated, e.g. the pair of levels Yen and Otsu.

- The regions outside the binary masks are cleared in two *duplicates* of the original image.

- The *Gray Value* of the baseline-level is subtracted from the images segmented by these first two algorithms Yen and Otsu.

- The two segmented images are Gaussian filtered with radiuses σ of which the first, the lower level image, is pre-determined and has a value in the range $50\ldots100$.

- The second, higher level image will be Gaussian filtered with a σ that has a value determined – from the first radius σ – by the *ratio* of the two levels, e.g. 0.86.

- The two resulting Gaussian filtered segmented images are then *subtracted* from each other, creating the first portion of the correction image.

- The *second* pair of `Auto Threshold` levels is next determined, for example the pair of levels Otsu and Shanbhag.

- The threshold levels and the concomitant binary masks are determined from the *Gray Values* of the *original* image. However, the next threshold level is always calculated from the image cleared by the binary mask of the *previous* level, utilizing the option `ignore black` in the `Auto Threshold`-tool.

- The same procedure as for the first pair is repeated, and the second portion of the correction image is formed and then added to the first.

- The third pair of threshold levels could be for example the pair of Shanbhag and Shanbhag, for which the higher level is calculated using the binary mask of the lower. The resulting correction image is again summed with the previous.

- The procedure can be continued to ever higher levels, resulting in ever thinner edge-areas of the metal plate to be segmented and processed.

- The dark artefacts can additionally be utilized in the stepwise formation of the correction image, since they always emerge alongside the bright artefacts and hence delineate the outer borders of the actual brightness. By inverting the dark artefacts and performing similar Gaussian filtering on them, the resulting surface of brightness can be remodeled to resemble the bright artefacts more closely.
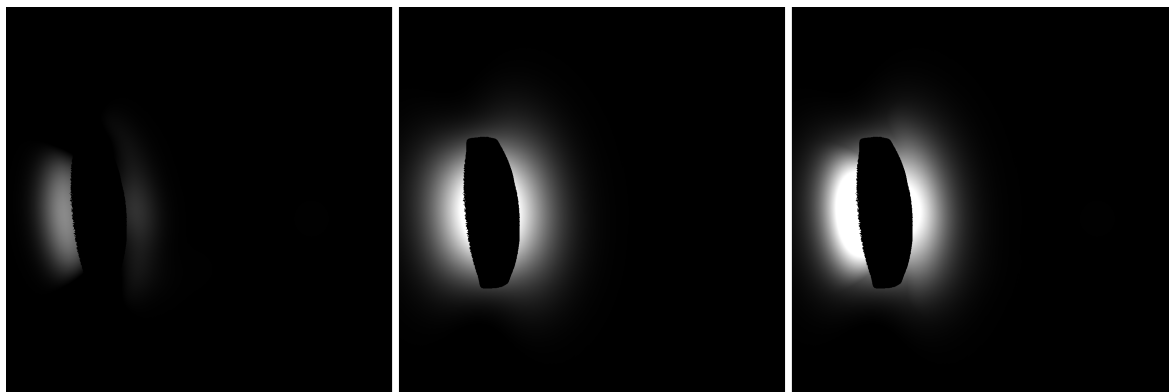
Figure 5.8: At left, the first portion of the correction image for the slice from Figure 5.1 produced by the pair of threshold algorithms Yen and Otsu. **At center**, the second portion of the correction image produced by the threshold algorithms Otsu and Shanbhag [40]. **At right**, the summed image of first and second images. The metal plate at the center of the images has been removed with Otsu. More threshold pairs can be added to form the final correction image, which is at the center of the next Figure 5.9.

As has already been mentioned, the procedure can be continued far beyond the first two pairs in Figure 5.8. For the images presented in Figure 5.9, altogether nine pairs of thresholdings were performed. The higher thresholdings isolate a continuously diminishing region at the very corners of the metal plate, and simultaneously the *ratios* of the *Gray Values* of the threshold levels approach one, which consequently causes the Gaussian filter radiuses σ to approach each other. The pre-determined radiuses σ for the *lower* thresholds (in a pair), from which the radius σ is determined for the higher threshold, are experimentally defined though (forming a series 50,100,25,12,10,...), and therefore may not be the proper values for all different pairs of threshold levels.
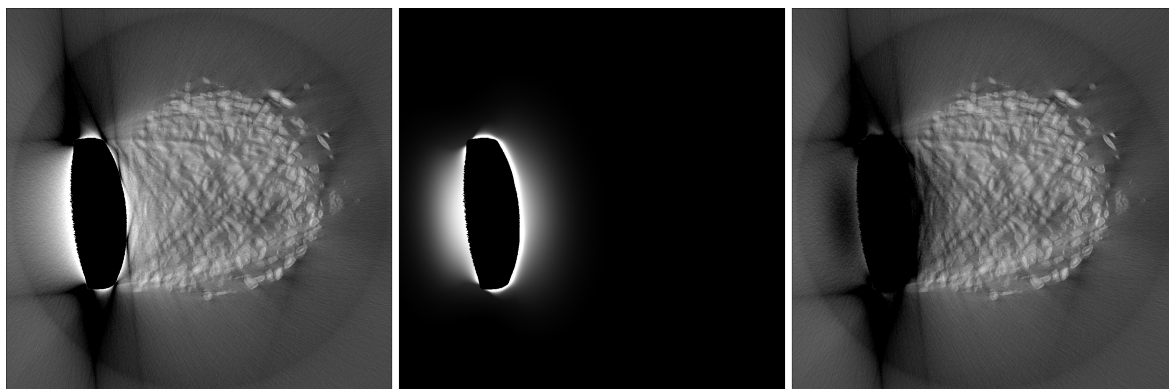
Figure 5.9: At left, the original slice from Figure 5.1 with the metal plate cleared by Otsu. **At center**, the final correction image formed by 9 consecutive thresholding pairs and the corresponding sequential Gaussian filtering and subtractions. **At right**, the corrected original image, from which the excessive brightness emanating from the metal has in practice been completely removed. However, traces of other types of artefacts still remain on the lower edge of the sample.
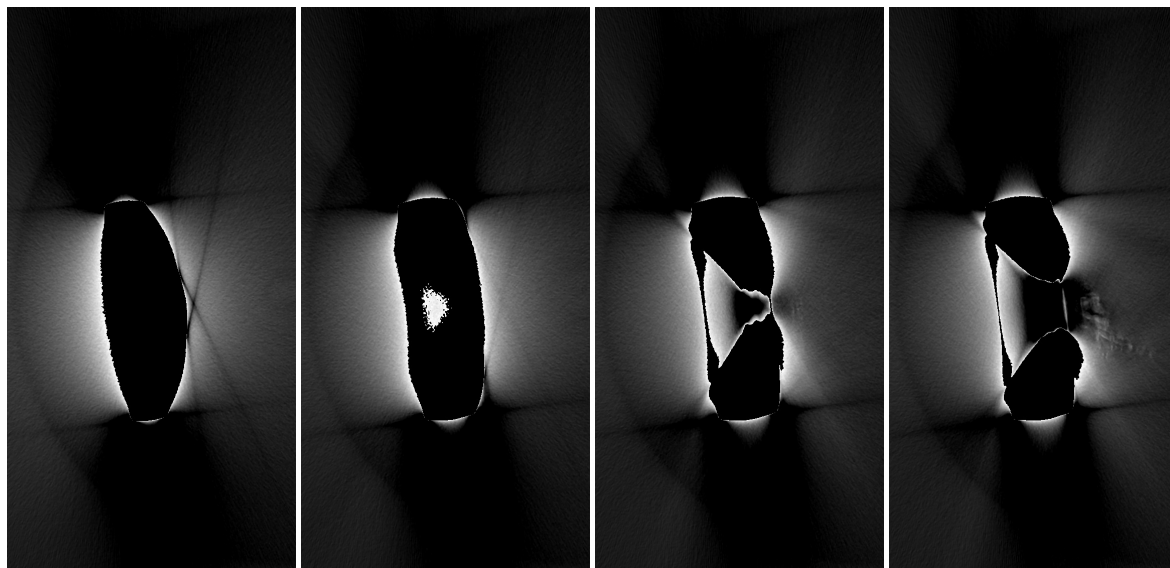
Figure 5.10: A series of images from sample D15, which contains a portion of the metal plate that is not adjacent to a femur or any other objects. **At far left**, the main artefact emanating from the metal reaches furthest in this portion of the plate. **At center left**, as the screw hole approaches, the artefact begins to diminish. **At center right**, the screw hole is clearly visible and the shape of the artefact has changed. **At far right**, the reach of the artefact has diminished substantially.
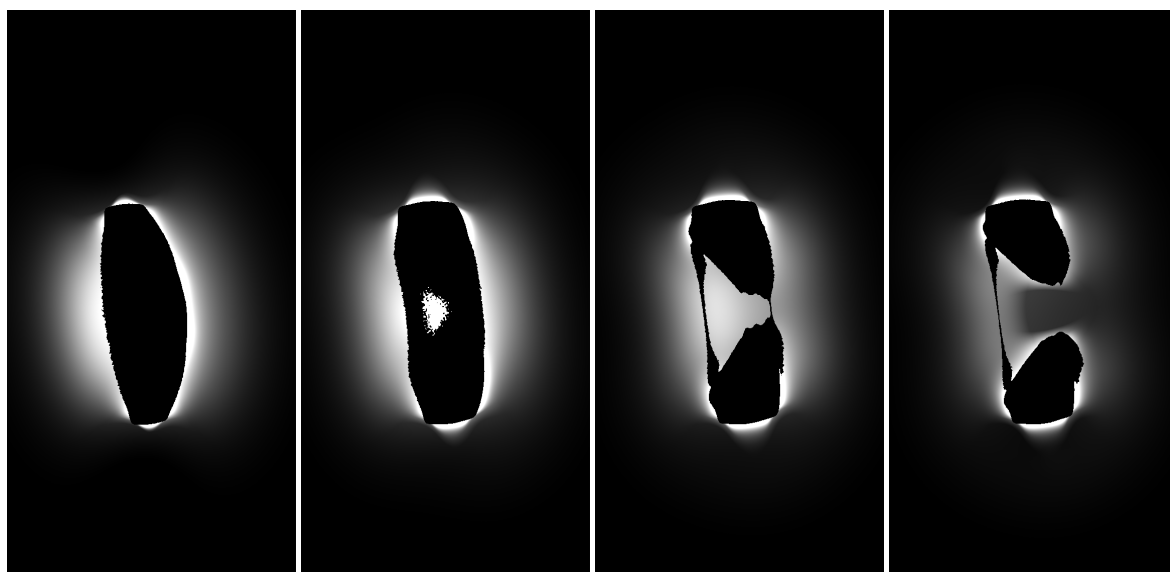
Figure 5.11: A series of correction images created by the method. **At far left**, the correction has a similar form as the main artefact in Figure 5.10. **At center left**, as the screw hole approaches, the correction begins to diminish in accordance with the actual artefact. **At center right**, the screw hole is clearly visible and the shape of the correction begins to alter. **At far right**, the reach of the correction has diminished substantially in accordance with the artefact. As this Figure demonstrates, the correction seems to have an intrinsic capability to adjust to the altering shape and reach of the artefacts. The parameters of the method can easily be adjusted to alter the maximum reach and the attained shape of the created surfaces of brightness, hence refining the resulting correction image.

5.3   Image Segmentation

Image segmentation is an integral part of image processing in many disciples of science, and in fact the segmentation of images into their constituent elements or objects can be regarded as being in essence the objective of the entire imaging procedure in, for example, many areas of biomedical research.

Segmentation can be accomplished by various different methods and techniques, for example by thresholding the image based on the brightness of its constituent objects and classifying the obtained binary masks according to their content.

In the rabbit femur samples of this Thesis, however, the fundamental content, i.e. bone, can not easily be thresholded and thus segmented, since the intrinsic brightness of the trabecular bone is very close to the brightness of the cortical bone – which in addition is often in close contact with the trabecular structures – and therefore most thresholding algorithms cannot distinguish between them.

Therefore, alternative methods must be used to perform a successful segmentation in images that contain these two types of bone, and a viable method to separate complex three-dimensional objects, that may in addition be intertwined amongst each other, is the technique of *morphological filtering* [28].

Morphological filtering is – as the name implies – based on exploiting the subtle differences in the *shapes* and *textures* of objects within a sample [28], and it is therefore especially well suited to perform a segmentation for samples that contain objects with similar or identical brightnesses [28].

An essential tool in morphological filtering is a *gray-scale Dilation* and *Erosion*, which resembles *binary* Dilation and Erosion to a certain degree, but with the obvious distinction that it is performed on images with a continuous scale of innate brightness. The gray-scale Dilation and Erosion are based on the utilization of *maximum* and *minimum* filtering, which operate by changing the values of brightness in voxels according to the maximum or minimum value of other voxels in their immediate proximity [30].

By a combination of the morphological Erosion and Dilation operations, the morphological operations *Opening* and *Closing* can be performed [28]. In these operations the brightness of an object can be considered as a 3D-surface, which is approached from above or below by a *structuring element* that can be a small disk or some other similar geometrical entity [28].

The element then closes all the *gaps* on the surface to which it cannot reach, thus performing an Opening or a Closing operation, depending on the direction of approach. This newly created closed or opened surface can then be utilized in various additional operations, one of which is the *Black top-hat* operation that is utilized in the following Subsections.
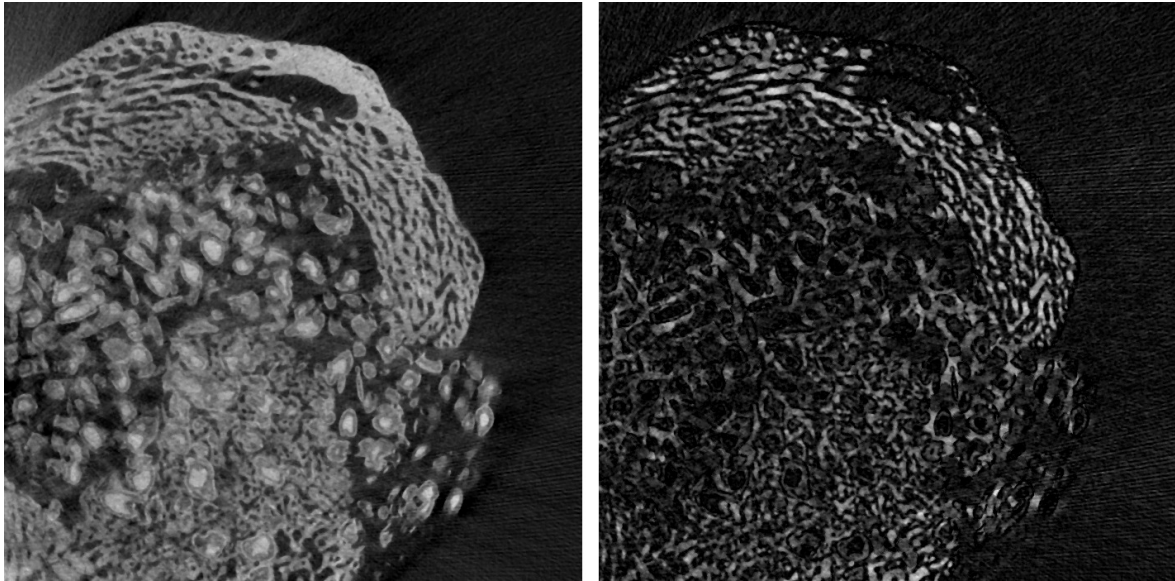
Figure 5.12: At left, an arbitrary slice from sample D31. **At right**, the *Black top-hat* operator [28] enhances the thin regions in between the *trabecula* of the newly formed bone.

5.3.1   Segmentation of the Trabecular Structures

The cross-section of a three-dimensional network of trabecular bone – or any other material with a similar structure – on the two-dimensional slices appears as a net of interconnected *ridges* and *holes* that form between them, when the values of brightness of a 2D-slice are in turn regarded as a 3D-surface. Then, by performing the morphological Closing operation, in which a disk with a radius of a few pixels can be pictured to move across the surface and fill all the tiny holes to which it cannot fit into, the net is in essence closed if the relative size of the disk exceeds that of all the holes.

However, if the *original* slice is next *subtracted* from the newly closed surface, most pixels then obtain a value of zero, but the pixels that were originally on the site of the holes are then in a sense elevated to a new position and are all that remain from the Closed surface. By this operation it is therefore possible to in practice *invert* the *gaps* between the original net of material, and simultaneously remove the net, in this case the trabecular bone. This is the Black top-hat operation, and it can be utilized to *identify* the trabecular structures on the images.

At the length scales of the trabecular bone in the samples, a Black top-hat [28] operation performed with a disk radius of 7 pixels (by utilizing consecutive maximum and minimum filters) leaves to the remaining structure – after the subtraction of the original image – enough elevated areas so that the structure can be Closed again by the utilization of consecutive maximum and minimum filters with a disk radius of 5 pixels. This new uneven 3D-surface can then be thresholded with `Auto Threshold`-function Triangle. If the resulting binary mask is next selectively combined (by the

binary operator AND) with a binary mask containing in essence all pixels that are *not* background (the Default-function of *ImageJ*) the resulting binary mask seems to trace the trabecular structures quite precisely.
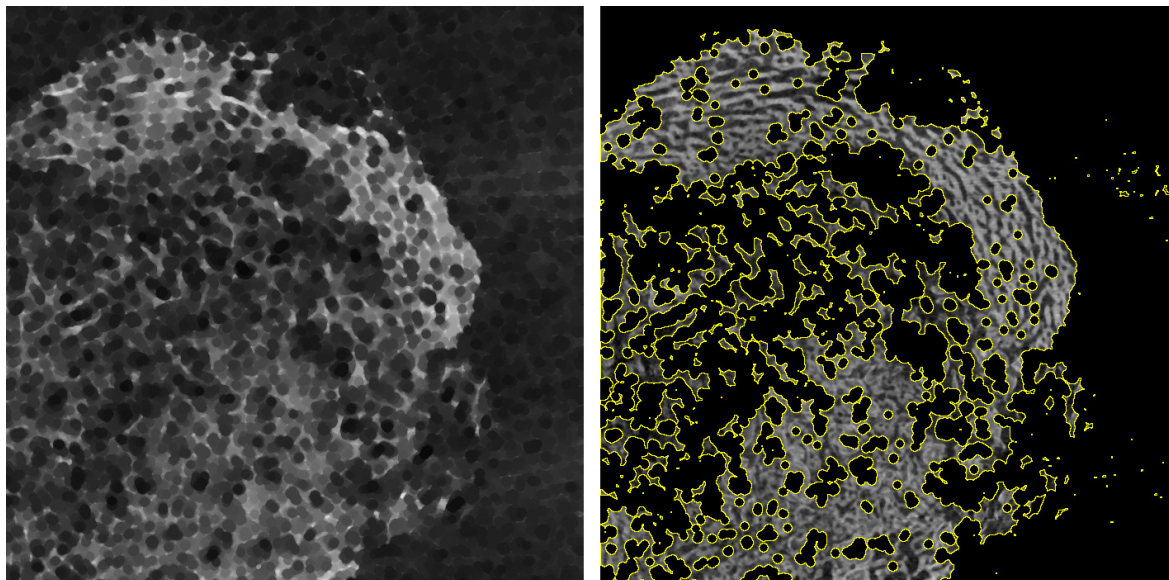

Figure 5.13: At left, as the *Black top-hat* image from Figure 5.12 is Closed and the resulting image is thresholded by `Auto Threshold` Triangle, the binary mask delineates the trabecular structure quite precisely, **at right**. Obviously, not all objects contained within the binary mask are portions of trabecular bone, but on average the method appears to function properly. The length scale of the trabecular structures that the method is able to identify can in principle be adjusted by the parameters of the morphological operations.

5.3.2   Segmentation of the Dense Granules

The densest glass granules and the cortical bone can easily be segmented with `Auto Threshold`-function Max Entropy. Alongside these, however, the most dense trabecular bone is also included in the binary mask. By inverting the previously obtained binary mask for the trabecular bone, i.e. the *morphological* trabecular structure, and using the binary operator AND, the portion of the trabecular bone can be subtracted from the Max Entropy mask. By performing a series of mild binary Openings, the mask can be cleared of everything but the granules and the cortical bone.

As the granules are considerably smaller objects than the cortical bone or even portions of it, they may easily be segmented from each other by the use of for example the `Analyze particles`-tool of *ImageJ*, which can distinguish and categorize separate objects by their size. On occasion though, the granules may be connected to the cortical bone and their separation may prove to be difficult.
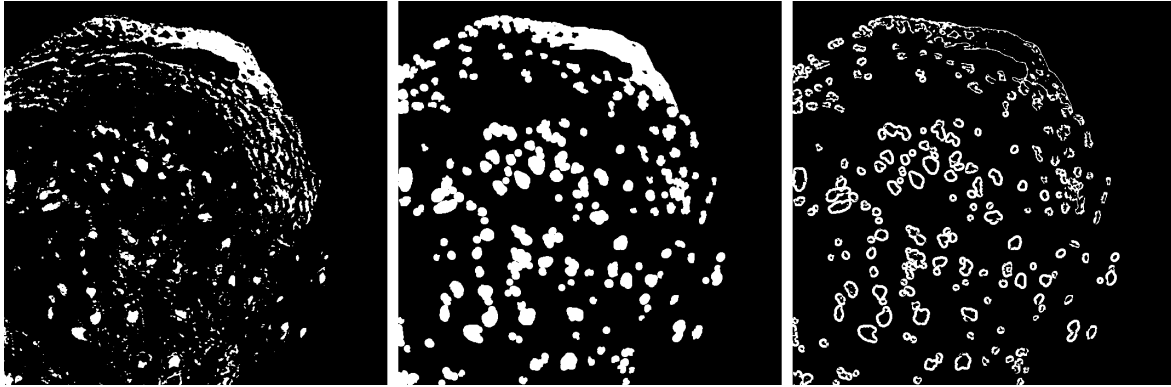
Figure 5.14: At left, a binary mask obtained by thresholding the image from Figure 5.12 with `Auto Threshold`-algorithm Max Entropy. **At center**, the same binary mask that has been Dilated, after the binary mask of the trabecular structures, obtained separately, has in effect been subtracted from it. **At right**, the binary mask from the center, from which the binary mask on left has been subtracted by inversion and binary operator AND. The separated thin regions around the granules can next be utilized in *identifying* the exact locations of the potential surface layers contained within the masks. Subsequent thresholding could then accomplish the segmentation of the silica gel layers – and possibly any HCA layers that were not yet included in the segmentation of the trabecular structures.

5.3.3   Segmentation of the Granule Shells and Silica Layers

A segmentation scheme to isolate the surface layers (Section 3.5) of the granules could feasibly be based on the brightness of these structures. However, the brightness of the HCA-layer – by definition – resembles that of bone, and therefore their separation from other objects may prove to be difficult based on brightness alone. Also, their *identification* as surface layers may not be straightforward.

The dense granules may, however, be utilized in identifying the locations of the surface layers of silica gel and the shells of HCA, since by definition the surface layers envelop the granules. As the dense granules at the center of the layered structure can be thresholded, as described in the previous Subsection, they may be useful to determine the proper locations of the surfaces.

By Dilating the thresholded granules and then using the binary operator AND to identify the approximate region of the surface layers, a subsequent thresholding of the contents of the dilated binary mask may prove to be useful in segmenting the layers, although the method of morphological *reconstruction* [28] may be superior in precision.

This segmentation scheme would then also categorize the surface layers to those that are positioned on top of a dense, bright granule that has not yet dissolved substantially, and to those that are located on top of granules that are already to a large extent dissolved, which could mean that the silica layer has in fact advanced to the center of the granule.
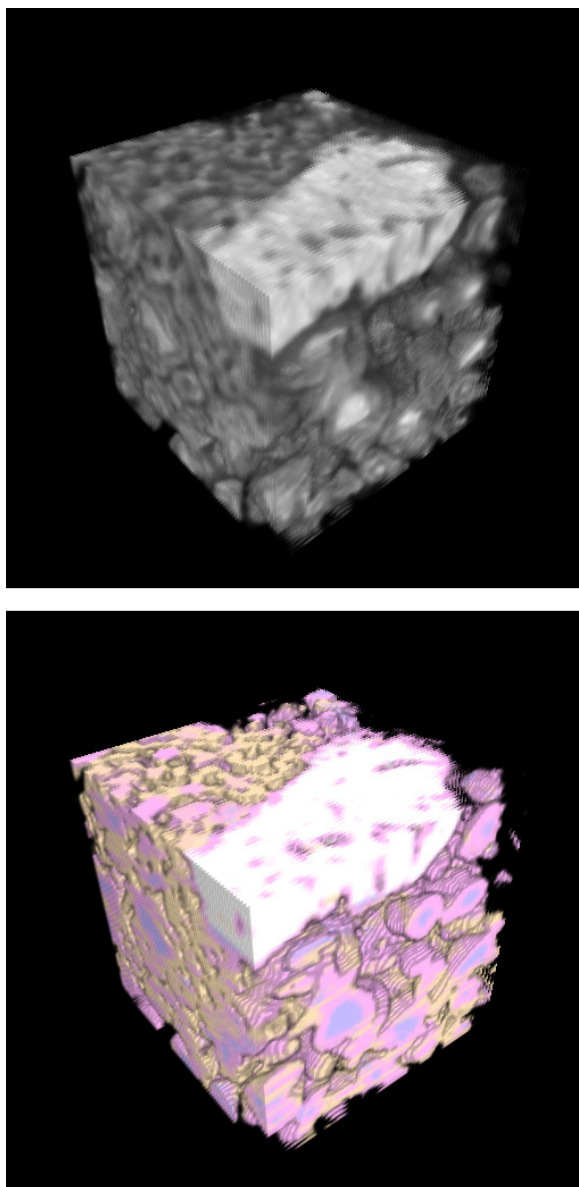
Figure 5.15: A 3D-visualization of a small $150 \times 150 \times 150$-voxel cube from sample D31 at the center of the scaffold near the edge of cortical bone. **Upper** image is in grayscale, showing a portion of cortical bone and partially dissolved granules surrounded by trabecular bone. **Lower** image is a result of segmentation, performed first by morphological filtering to separate the trabecular structures (**brown**), and then by thresholding the regions of the cortical bone and granules. Subsequently the cortical bone (**white**) and the granules (**purple**) are separated according to their *size*. In this image, all the rest of the pixels are classified as belonging to the silica gel layers (**pink**), although it is obvious that not all pink regions belong to the reaction layers. Therefore, the segmentation should be refined by determining the regions that are directly adjacent to the granules, by either Dilating the granules or by utilizing e.g. the method of *morphological reconstruction* on them, and subsequently thresholding the dilated region to isolate the silica gel layer and any potential layers of HCA that are not connected to the trabecular structures.

6. Discussion and Conclusions

The topic of this Thesis, the reduction of image artefacts in x-ray microtomography images and the subsequent segmentation of the resulting images, is a topic of great importance in the field of image processing in general. The quantitative analysis of x-ray microtomography images relies principally on the segmentation of the 3D-images into regions of interest that may then be measured and analysed, but the success of the segmentation depends directly on the effectiveness of the artefact reduction procedure. Therefore, all the methods introduced in the Thesis are intrinsically interconnected and should hence be applied in conjunction with each other.

As for the segmentation of the images, the multi-stage procedure that was presented in Section 5.3 is intended to be a preliminary segmentation scheme only, to be refined – perhaps – indefinitely by the addition of ever more detailed steps into the process, depending on the samples measured and the information that is expected to be extracted from them. The step to separate the trabecular bone from the rest of the sample utilizing morphological filtering (Section 5.3), however seems to be more universal in a sense that the parameters of the process can be easily adjusted to accommodate for the different length scales of the trabecular bone, for example to that of a human. By developing the procedure further, an efficient image processing tool could perhaps be created, to be added to the wide tool-kit of segmentation techniques. Same applies to the artefact reduction method introduced in Section 5.2.3, provided that this post-processing method can be generalized to function similarly on any reconstructed image containing metal artefacts.

The reduction or removal of metal artefacts on x-ray (micro)tomography images has for the past few decades been focused mainly on novel reconstruction techniques, and the post-processing methods applicable to images that are already reconstructed have been gaining ever declining attention. This may be due to the fact that no new methods have been introduced in many years for the post-processing of images, and on the other hand, the novel reconstruction methods have proven to be quite efficient, enabling for example a selective *exclusion* of the metal from the original raw data [26].

However, there would still be great demand for an elementary, yet simultaneously efficient method to reduce metal artefacts on x-ray (micro)tomography images that are

reconstructed using the traditional Filtered Back-Projection method, which is still a standard integrated method on many turn-key μCT systems and apparatuses. For example many tomography, i.e. CT-scan, systems in hospitals and medical centers use the traditional methods – with numerous extensions and enhancements incorporated into the original algorithm, of course – as a default choice on their systems.

Therefore, the method that was introduced in this Thesis could perhaps someday find use in the wider tomography community. However, a thorough testing and validation of the method should naturally first be conducted, followed – or preceded – by the development of a solid theoretical foundation delineating and conceivably even explaining the functionality of the method. For the time being, a preliminary explanation on at least the principles behind the method may however be feasible.

As the x-ray beam passes through the measured object, some portion of it always scattered or absorbed by the atoms of the sample, reducing the amount of x-ray photons (per each line of radiation) reaching the detector (Subsection 2.2.1). This, of course, is the fundamental working principle of the method in the first place, but in samples that contain relatively dense materials, or materials containing heavy elements, the same phenomenon also contributes to the formation of the artefacts in the reconstructed images.

Due to the polychromatic nature of the x-ray radiation produced by standard x-ray tubes, the energy spectrum of the radiation, which is spread out to a wide range of energies, causes the detector – in itself insensitive to the energy of individual x-ray photons – to receive a disproportionate amount of high-energy photons which have been able to penetrate the dense portions of the sample, for example the parts containing metal (Subsection 2.1.4). As the sample is then rotated and the overall thickness of the dense material, through which the x-ray beam passes, hence alters due to the varying orientation of the sample, the disparity in the number of received photons on different rotation angles due to the beam hardening -effect causes an inconsistency in the data from which the reconstruction is calculated. In situations in which the (average) energy of the radiation, i.e. the voltage of the x-ray tube, must be adjusted to a level that enables the objects of interest to be discerned and recognized, the resulting (metal) artefacts can be quite formidable.

The metal artefacts themselves seem to consists of two separate distinguishable portions which are summed up in the reconstructed image. The first portion, the main beam hardening -portion, manifests itself as the *cupping-effect* -phenomenon that causes the very edges of the metal to become excessively bright in relation to their true density. It seems to have a tendency to concentrate on the shorter edges of the metal plate (on the transverse slices, see Figures 5.1 and 5.4, at left).

The second portion of the metal artefacts manifests itself as a surface of excessive

brightness emanating from the metal, when the brightness is considered as height of a 3D-surface. This portion may be caused by the same mechanism that gives rise to the cupping-effect, or there could be a different mechanism altogether behind it. For example *scattering* may be responsible for the emanating surface of brightness, due to the *recoiled* photons that alter their path inside the metal, and consequently exit the material and reach the detector following a trajectory that is slightly deviated from their initial path. This may cause inconsistencies in the measurement data, and the artefact then forms.

Regardless of the cause of the bright artefact, it seems to emanate furthest from the *long* edges of the metal plate (Figure 5.10), whereas the cupping-effect artefact appears to be brightest at the *short* edges of the plate, with the most bright portion at the corners (Figures 5.1 and 5.4, at left).

Then, as the metal plate is thresholded consecutively and the segmented parts are Gaussian filtered and subtracted from each other, the higher threshold always isolates the area nearest the short edge and the corners. As this smaller Gaussian filtered area is then subtracted from the other, larger Gaussian filtered area, the smaller always *supresses* the resulting broad surface of the correction image near the short edges. As a result, a correction image that resembles the original bright artefact is formed, not necessarily because the two types of artefacts are initally interrelated, but because they tend to form on different sides of the metal plate. As a conclusion, it could then be assumed that the *geometry* of the plate is the defining factor in the functionality of the method.

As the primary objective in the development of the methods presented in this Thesis was to create a mathematical tool to reduce the artefacts which *overlap* the region of the sample that contains the granules and the bone, the reduction of the artefacts *within* the region of the metal itself was intentionally left essentially unexplored. However, it would seem that the Gaussian surfaces which are calculated from the thresholded regions, and that are in essence *cleared* from the region of the actual metal to create the final correction image, could in fact be usable themselves to reduce the cupping-effect present on the metal itself. Coincidentally or not, the overall shape and form of the cupping-effect on the edges of the metal in fact resembles that of an *inverted* Gaussian surface.

Then, as more and more correction images are calculated by methodically subtracting the Gaussian filtered, segmented images of pairs of consecutive thresholdings, and then adding all these together, it could be feasible that eventually a surface would form which corresponds directly to the surface formed by the beam hardening effect inside the metal parts. Naturally, achieving this would require a considerable amount of further testing and a progressive refinement of the method.
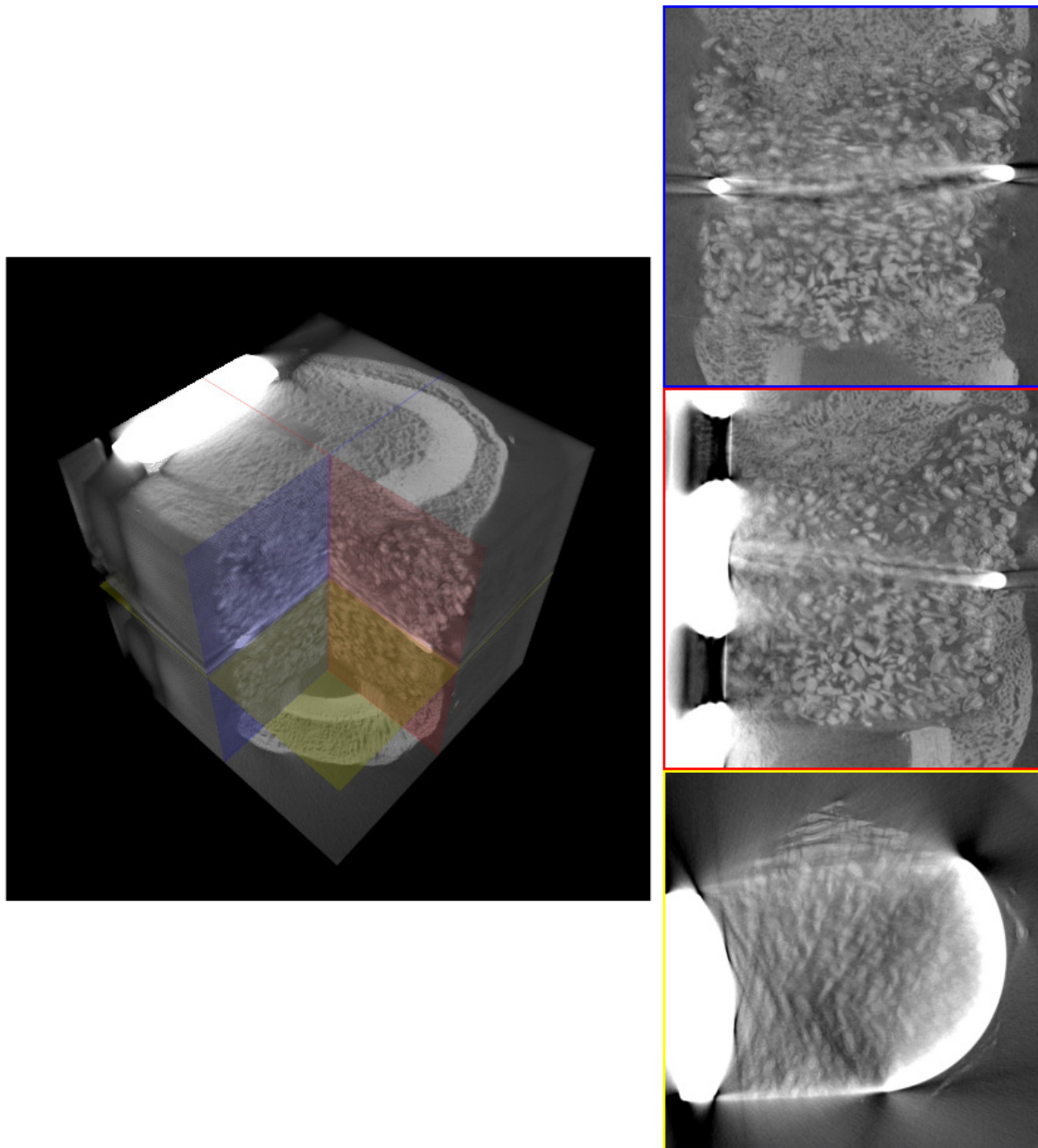
Part V

Appendices

Appendix A. Image Processing Supplement

Figure A.1: At left, a 3D-visualization of a cubic ($800 \times 800 \times 800$)-voxel stack – cropped from the original ($1128 \times 1128 \times 1152$)-voxel stack – from which approximately a quarter has been removed for illustrative purposes. The brightness of the original stack has been adjusted for an enhanced contrast. The **blue**, **red** and **yellow** planes in the 3D-visualization depict the *coronal*, *sagittal* and *transverse* planes of the stack, respectively. For comparison, a radiograph of the same sample, D13, is provided in Figure 4.2. **At right**, three individual slices extracted from the locations of the blue, red and yellow planes are presented. Cross-sections of the metal wire – and artefacts – can be observed on all slices.

The three-dimensional image produced by the reconstruction process – following the x-ray (micro)tomography measurements – can be regarded as being a large *stack* of two-dimensional *slices* on top of each other. Equivalently, the slices can be considered to be *extracted* from the stack, since their orientation does not necessarily have to be cross-sectional in the *transverse* direction or plane, and instead for example *sagittal* or *coronal* cross-sections can be produced. In fact, through *rotations* and other *transformations* of the stack, almost any orientation for the slices can be produced, though by convention a transverse plane is often preferred.

Depending on the task at hand, the extracted slices can then be processed or analysed as semi-2D-images with a thickness of one voxel in the z-direction, or, with advanced image processing techniques, the entire 3D-image can be processed at once. Furthermore, almost any arbitrary *volume* from the original stack can be selected and reproduced for processing and analysis, as most image processing methods allow for a copy of the original data, i.e. a *duplicate* of the 3D-image to be used. For example, the creation of a *binary mask* relies on a duplicate of an image to determine discrete *regions* of voxels – based on e.g. their innate brightness – that are then converted to either black or white, regions which can then be utilized in further processing by reverting to the original, unmodified image (from which more copies can be made as needed).

All original 3D-images produced by the reconstruction process were stacks of size $1128 \times 1128 \times 1152$ voxels. The size of an individual cubic voxel was $15\mu m^3$, and hence the width and height of an individual slice from the xy-plane was 16.92mm. The *bit-depth* of the images was 16 bits, thus producing a *Gray Value*-scale of $0 \ldots 65535$. The various objects of interest in the images, i.e. the bioactive glass granules and the newly formed bone, acquired values approximately at the middle of the scale ($30000 \ldots 40000$), while the dense and bright metal attained values towards the upper end of the scale. Many images presented in this Thesis are *adjusted* in their brightness and contrast by determining a minimum and maximum value for the existing brightness, and scaling the portion in between these values to new values that span the entire scale $0 \ldots 65535$. A portion of information is hence inevitably lost in the imprinted Figures of this Thesis, but the presentation of the images often requires this adjustment to be made. At the stage of the actual image processing these types of adjustments were not conducted.

For processing the images, the freely distributed software *ImageJ* (version 1.52p) and its auxiliary *Fiji*-package was used [30][39]. Throughout this Thesis, the image processing tools of *ImageJ* will be referred to in a `typescript` notation.

Bibliography

[1] S. R. Stock. X-ray microtomography of materials. *International Materials Reviews*, 44(4):141–164, 1999.

[2] Eric N. Landis and Denis T. Keane. X-ray microtomography. *Materials Characterization*, 61(12):1305–1316, 2010.

[3] Alessandra Giuliani and Alessia Cedola. *Advanced High Resolution Tomography in Regenerative Medicine*. Springer, Cham, Switzerland, 2018.

[4] Delia S. Brauer. Bioactive glasses - structure and properties. *Angewandte Chemie-International Edition*, 54(14):4160–4181, 2015.

[5] N. A. P. van Gestel, J. Geurts, D. J. W. Hulsen, B. van Rietbergen, S. Hofmann, and J. J. Arts. Clinical applications of S53P4 bioactive glass in bone healing and osteomyelitic treatment: A literature review. *BioMed Research International*, Volume 2015(Article ID 684826):1–12, 2015.

[6] Jerrold T. Bushberg. *The essential physics of medical imaging*. Wolters Kluwer Health/Lippincott Williams & Wilkins, Philadelphia, 2012.

[7] Mary L. Bouxsein, Stephen K. Boyd, Blaine A. Christiansen, Robert E. Guldberg, Karl J. Jepsen, and Ralph Mueller. Guidelines for assessment of bone microstructure in rodents using micro-computed tomography. *Journal of Bone and Mineral Research*, 25(7):1468–1486, 2010.

[8] A. C. Kak and M. Slaney. *Principles of Computerized Tomographic Imaging*. IEEE Press, (Electronic Copy 1999), 1988.

[9] Willi Kalender. *Computed tomography: fundamentals, system technology, image quality, applications*. Publicis, Erlangen, 2005.

[10] Jiang Hsieh. *Computed tomography: principles, design, artifacts and recent advances*. Wiley Interscience, Hoboken, N.J., 2009.

[11] Thorsten Buzug. *Computed tomography: from photon statistics to modern cone-beam CT.* Springer, Berlin, 2008.

[12] Mark Haidekker. *Advanced Biomedical Image Analysis.* John Wiley & Sons, Hoboken, N.J., 2011.

[13] S. R. Stock. Recent advances in x-ray microtomography applied to materials. *International Materials Reviews*, 53(3):129–181, 2008.

[14] E. Maire and P. J. Withers. Quantitative x-ray tomography. *International Materials Reviews*, 59(1):1–43, 2014.

[15] Abiy Wubneh, Eleni K. Tsekoura, Cagri Ayranci, and Hasan Uludag. Current state of fabrication technologies and materials for bone tissue engineering. *Acta Biomaterialia*, 80:1–30, 2018.

[16] Wenhao Wang and Kelvin W. K. Yeung. Bone grafts and biomaterials substitutes for bone defect repair: A review. *Bioactive Materials*, 2(4):224–247, 2017.

[17] Lutz-Christian Gerhardt and Aldo R. Boccaccini. Bioactive glass and glass-ceramic scaffolds for bone tissue engineering. *Materials*, 3(7):3867–3910, 2010.

[18] Julian R. Jones. Review of bioactive glass: From Hench to hybrids. *Acta Biomaterialia*, 9(1):4457–4486, 2013.

[19] Richard Marsell and Thomas A. Einhorn. The biology of fracture healing. *Injury-International Journal of the Care of the Injured*, 42(6):551–555, 2011.

[20] Thomas A. Einhorn and Louis C. Gerstenfeld. Fracture healing: Mechanisms and interventions. *Nature Reviews Rheumatology*, 11(1):45–54, 2015.

[21] Nina C. Lindfors, Jouni T. Heikkila, Ilona Koski, Kimmo Mattila, and Allan J. Aho. Bioactive glass and autogenous bone as bone graft substitutes in benign bone tumors. *Journal of Biomedical Materials Research Part B-Applied Biomaterials*, 90B(1):131–136, 2009.

[22] N. C. Lindfors, P. Hyvonen, M. Nyyssonen, M. Kirjavainen, J. Kankare, E. Gullichsen, and J. Salo. Bioactive glass S53P4 as bone graft substitute in treatment of osteomyelitis. *Bone*, 47(2):212–218, 2010.

[23] Lorenzo Drago, Marco Toscano, and Marta Bottagisio. Recent evidence on bioactive glass antimicrobial and antibiofilm activity: A mini-review. *Materials*, 11(2):326, 2018.

[24] R. Bjorkenheim, G. Stromberg, J. Pajarinen, M. Ainola, P. Uppstu, L. Hupa, T. O. Bohling, and N. C. Lindfors. Polymer-coated bioactive glass S53P4 increases VEGF and TNF expression in an induced membrane model in vivo. *Journal of Materials Science*, 52(15):9055–9065, 2017.

[25] Robert Bjorkenheim, Gustav Stromberg, Mari Ainola, Peter Uppstu, Laura Aalto-Setala, Leena Hupa, Jukka Pajarinen, and Nina C. Lindfors. Bone morphogenic protein expression and bone formation are induced by bioactive glass S53P4 scaffolds in vivo. *Journal of Biomedical Materials Research Part B-Applied Biomaterials*, 107(3):847–857, 2019.

[26] Lars Gjesteby, Bruno De Man, Yannan Jin, Harald Paganetti, Joost Verburg, Drosoula Giantsoudi, and Ge Wang. Metal artifact reduction in CT: Where are we after four decades? *IEEE Access*, 4:5826–5849, 2016.

[27] Florence Loi, Luis A. Cordova, Jukka Pajarinen, Tzu-hua Lin, Zhenyu Yao, and Stuart B. Goodman. Inflammation, fracture and bone repair. *Bone*, 86:119–130, 2016.

[28] Pierre Soille. *Morphological Image Analysis*. Springer, Berlin, 2003.

[29] Michael Doube, Michal M. Klosowski, Ignacio Arganda-Carreras, Fabrice P. Cordelieres, Robert P. Dougherty, Jonathan S. Jackson, Benjamin Schmid, John R. Hutchinson, and Sandra J. Shefelbine. BoneJ free and extensible bone image analysis in ImageJ. *Bone*, 47(6):1076–1079, 2010.

[30] T. Ferreira and W. S. Rashband. ImageJ User Guide - IJ 1.46.

[31] Milla Kalliokoski. *X-ray spectrum of the Microtomography Laboratory's x-ray tube.* (Laboratory exercise), 2017.

[32] J. H. Hubbell and S. M. Seltzer. Tables of x-ray mass attenuation coefficients and mass energy-absorption coefficients from 1 keV to 20 MeV for elements Z = 1 to 92 and additional substances of dosimetric interest, https://www.nist.gov.

[33] M.J. Berger et al. XCOM: Photon cross sections database, https://www.nist.gov.

[34] Martin Stauber and Ralph Muller. *Micro-Computed Tomography: A Method for the Non-Destructive Evaluation of the Three-Dimensional Structure of Biological Specimens. In: Westendorf J.J. (ed.) Osteoporosis. Methods In Molecular Biology, vol 455.* Humana Press, 2008.

[35] Gurbinder Kaur, O.P. Pandey, K. Singh, Dan Homa, Brian Scott, and Gary Pickrell. A review of bioactive glasses: Their structure, properties, fabrication and apatite formation. *Journal of Biomedical Materials Research A*, 102A(1):254–274, 2014.

[36] Olli-Matti Aho, Petri Lehenkari, Jukka Ristiniemi, Siri Lehtonen, Juha Risteli, and Hannu-Ville Leskela. The mechanism of action of induced membranes in bone repair. *Journal of Bone and Joint Surgery-American Volume*, 95A(7):597–604, 2013.

[37] Hugo R. Fernandes, Anuraag Gaddam, Avito Rebelo, Daniela Brazete, George E. Stan, and Jose M. F. Ferreira. Bioactive glasses and glass-ceramics for healthcare applications in bone regeneration and tissue engineering. *Materials*, 11(2530), 2018.

[38] Alastair N. Cormack. *The Structure of Bioactive Glasses and Their Surfaces. In: Julian Jones and Alexis Clare (ed.) Bio-Glasses: An Introduction.* John Wiley & Sons, Hoboken, 2012.

[39] J. Schindelin, I. Arganda-Carreras, and E. Frise. Fiji: an open-source platform for biological-image analysis. *Nature Methods*, 9:676–682, 2012.

[40] M. Sezgin and B. Sankur. Survey over image thresholding techniques and quantitative performance evaluation. *Journal of Electronic Imaging*, 13(1):146–168, 2004.